HIGH-RESOLUTION FACIES ANALYSIS AND REGIONAL CORRELATION OF THE
UPPER CRETACEOUS JUANA LOPEZ MEMBER OF THE MANCOS SHALE,
NEW MEXICO

By MONICA WIERCIGROCH, B.Sc. (Hons.)

A Thesis Submitted to the School of Geography and Earth Sciences in Partial Fulfilment of the
Requirements for the Degree Master of Science

McMaster University MASTER OF SCIENCE (2018) Hamilton, Ontario (School of Geography and Earth Sciences)

TITLE: High-resolution Facies Analysis and Regional Correlation of the Upper Cretaceous Juana Lopez Member of the Mancos Shale, New Mexico

AUTHOR: Monica Wiercigroch, Honours B.Sc. (McMaster University)

SUPERVISOR: Dr. Janok P. Bhattacharya

NUMBER OF PAGES: x, 87

Abstract

Fine-grained clastic sediments make up the gross lithology in interior basins of ancient epicontinental seas, such as the Cretaceous Western Interior Seaway. This study provides a high-resolution thin-bedded facies analysis and regional correlations to determine how the heterolithic units of the Juana Lopez Member of the Mancos Shale were transported and deposited in the San Juan Basin. Data for this study was obtained from outcrop observations in eleven measured sections, spanning a distance of 115 kilometers. Eleven facies are observed, four sequences and eleven parasequence sets are identified. A depositional model is determined through the high-resolution facies analysis, which suggests deposition on a proximal to distal mudbelt through multiple processes, including turbidity currents, hypopycnal plumes, wave enhanced sediment gravity flows (WESGFs), storm surges, tides and oceanic currents. Overall, the Juana Lopez is dominated by upward-shoaling parasequence sets, with an increasing number and thickness of sandstone dominated bedsets, suggesting regressive sedimentation with distal expressions of transgression found in two parasequence sets. The source of sediment is determined through 520 paleocurrent measurements and plaeogeographic data, and is determined to be transported by along-shelf currents, dominantly from proximal NE clastic wedges.

Table of Contents

List of Figures, Tables and Posters

1. Introduction

Fine-grained clastic sediments, composed of particles smaller than 62 µm, make up much of the gross lithology in interior basins of ancient epicontinental seas, such as the Cretaceous Western Interior Seaway (Fig. 1) (Schieber, 2016). These fine-grained sediments have been historically considered as being deposited as 'blankets' of sediment that settled slowly out of suspension, and the low levels of bioturbation and high TOC's have been used to infer anoxic conditions (Rhoads & Morse, 1971; Bromley & Ekdale, 1984; Savrda & Bottjer, 1987; Wignall, 1991; Wignall & Pickering, 1993; Martin, 2004; Potter et al., 2005; Laurin & Sageman, 2007). However, new models of mud transportation and deposition have shown that through flocculation, muds behave as larger aggregated particles that can be transported as bedload and form ripples (MacQuaker & Bohacs, 2007; Schieber et al., 2007; Schieber & Southard, 2009; Schieber, 2011; Yawar & Schieber, 2017). The processes that transport fine-grained sediments across shorelines and into interior basins include turbidity currents (which include slope failure and hyperpycnal flows), hypopycnal plumes, wave enhanced sediment gravity flows (WESGFs), storm surges, tides and oceanic currents (Dalrymple et al., 2003; Bhattacharya & MacEachern, 2009; Plint, 2014; Wilson & Schieber, 2014; Harazim & McIlroy, 2015; Li et al., 2015; Wilson & Schieber, 2015; Schieber, 2016).

Hypopycnal plumes are able to transport flocculated mud particles tens to hundreds of kilometers offshore (Schieber, 2016). Rivers feeding ancient epicontinental seas are known to be smaller in size due to their smaller drainage areas and potential sediment supply, since most of the continent was submerged under water. Therefore, it is unlikely for hypopycnal plumes to solely spread suspended sediment hundreds of kilometers offshore in epicontinental seas (Schieber, 2016). Sediments often settle out of hypopycnal plumes and can become remobilized

by waves and currents, and be moved further offshore as a liquid mud layer on slopes as small as 0.03° (Schieber, 2016). Turbidity currents, and WESGFs are able to carry sediment multiple kilometers offshore; however, the minimum slope requirement for these currents to support sediment in autosuspension is 0.7° (Bentley, 2003; Friedrichs & Wright, 2004; Friedrichs & Scully 2007; Bhattacharya & MacEachern, 2009; Schieber, 2016). Storms induce offshore flowing currents that move basinward and are deflected along-shelf by Coriolis effect, rather than gravity acting on the suspended sediment (Aigner & Reineck, 1982; Duke, 1990). Storm induced offshore transport can move mud up to about 400 km offshore, with a minimum slope angle of 0.03° (Schieber, 2016). With epicontinental seas having small regional bottom slopes (0.001° to 0.005°), and assuming a maximum water depth of 200 m, these processes are able to move fine-grained sediments on the order of hundreds of kilometers offshore and along-shelf, as summarized in Figure 2 (Schieber, 2016). Therefore, it is hypothesized that fine-grained sediment is transported offshore and along-shelf in ancient epicontinental seas by tidal and wind induced bottom current circulation (Schieber, 2016). Periods of lower sea level may also allow more seaward deposition, for example a 20 meter fall in sea level on a slope of 0.03° results in a 38 kilometer seaward translation of the shorleine (Schieber, 2016).
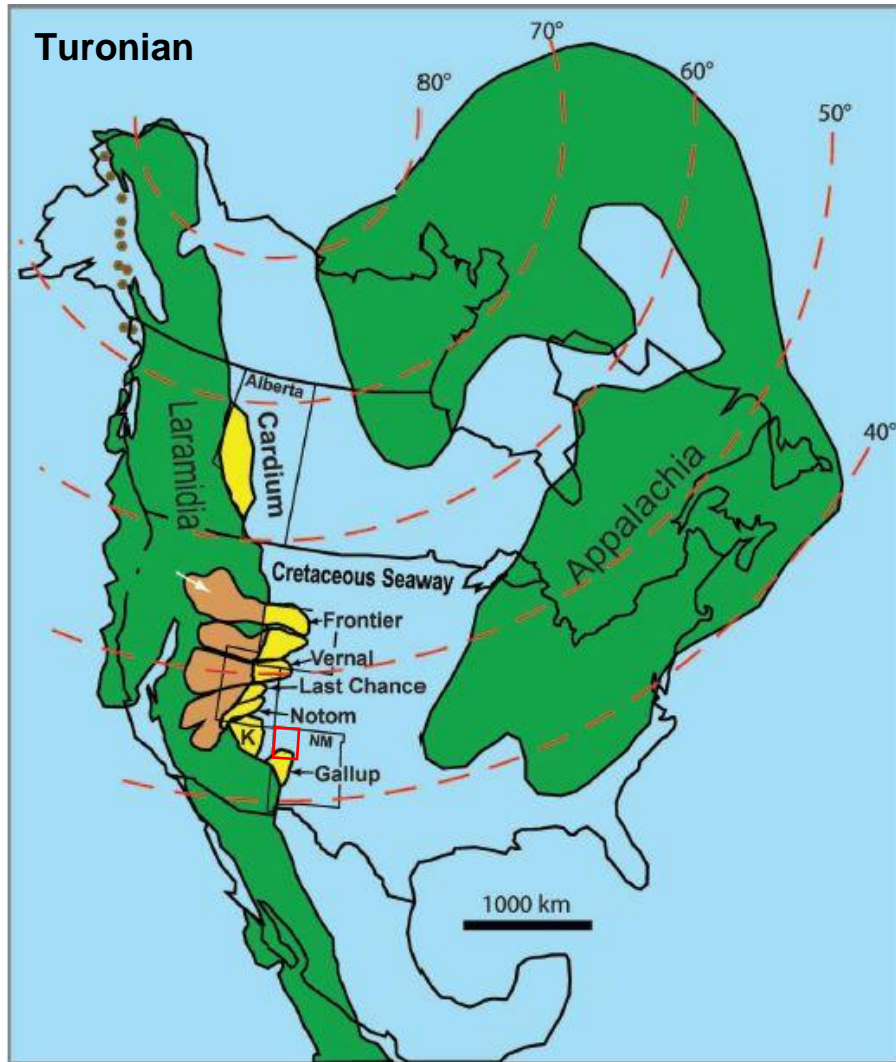
Figure 1- Cretaceous Western Interior Seaway showing the Cardium, Frontier, Vernal, Last Chance, Notom, Kaiparowits (K) and Gallup delta complexes in Turonian paleogeography (taken from Bhattacharya & MacEachern, 2009). Red box outlines the area under evaluation in this study.
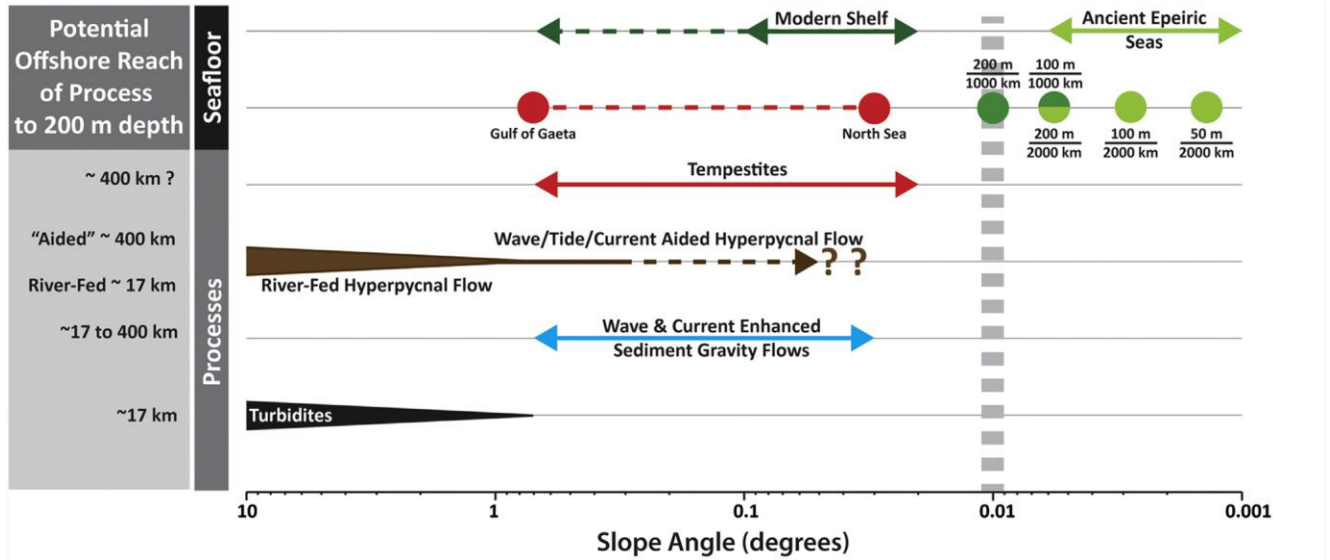
Figure 2- Potential offshore reach of mud transportation processes with a maximum water depth of 200 m and minimum necessary slope (on left), as well as their associated slope limits (on right) (taken from Schieber, 2016).

1.1 Significance and Objectives

High-resolution stratigraphic analysis, as well as the transportation and depositional mechanisms, of thin-bedded heterolithic facies have been overlooked and understudied due to the difficulty in the study of fine-grained outcrops. Fine-grained heterolithic outcrops are typically poorly exposed and easily weathered, causing them to seem featureless and homogeneous. However, high-resolution regional correlations of thin-bedded heterolithic facies play an important role in increasing production and profitability of unconventional hydrocarbon resources for the global energy market. This study focuses on the laterally extensive and well exposed cliff exposures of the thin-bedded, heterolithic Juana Lopez Member of the Mancos Shale in Shiprock, New Mexico, where a high-resolution facies analysis and regional correlation is possible.

This study has three primary objectives. The first objective is to provide a detailed facies analysis of the Juana Lopez Member, in the San Juan Basin. This facies analysis will serve as a model to evaluate the vertical and lateral facies variability in heterolithic units. Also, this facies

4

analysis will test the hypothesis of anoxic conditions, which is important in characterizing the source rock in the system. The second objective is to define and track key boundaries within the stratigraphic unit to determine whether coarsening-upward parasequence sets correlate regionally. This regional correlation will offer the oil and gas industry an analog that documents the lateral variability of heterolithic successions, which may consist of small scale reservoir seal pairs. The final objective is to establish a depositional model for the Juana Lopez Member, based on recent mud depositional models, such as Hart (2016), Schieber (2016), Birgenheier et al. (2017), and Li and Schieber (2018). The depositional model is interpreted based on the dominant depositional processes, as determined from the detailed facies analysis.

2. Geologic Setting

In the Late Cretaceous, western North America underwent crustal thickening through the subduction and compression of the Farallon plate beneath the North American plate (Livaccari, 1991; DeCelles, 2004). The plate subduction and convergence created linear north-south trending orogenic belts, including the Sevier fold-thrust belt (Livaccari, 1991; DeCelles, 2004; Yonkee & Weil, 2015). East of the Sevier belt, subsidence created a flooded basin, named the Western Interior Seaway (Fig. 1) in which hundreds to thousands of meters of sediment accumulated in the foreland basin of the seaway during the Cretaceous (Kauffman, 1984; DeCelles, 1994; DeCelles & Giles, 1996; Johnson, 2003). During the Late Cretaceous, the global annual mean surface temperature was approximately 6°C higher than current global temperatures and sea-floor spreading rates were increased, resulting in repeated flooding of the basin and a global eustatic highstand (Kauffman, 1977, 1985; Savin, 1977; Barron, 1983; Kauffman & Caldwell, 1993; Miller et al., 2005; Fluteau et al., 2007; Hay, 2008; Haq, 2014). The resulting Western Interior Seaway became completely invaded by Thethyan waters from the Gulf of

Mexico and Boreal waters from the Arctic Ocean (He et al., 2005; Kauffman, 1977). This epicontinental sea was up to 1,500 km wide with maximum water depths estimated to be about 200 m (Weimer, 1984; Kauffman 1985; Sageman & Arthurs, 1994; Schieber, 2016).

The Mancos Shale was deposited in the foredeep of the Western Interior Seaway, from 95 to 75 million years ago, as a mainly offshore marine shale fed by more proximal clastic shallow-marine and fluvial units at the margins (Nummedal, 1990). The Mancos Shale is divided into a lower and upper division and the Juana Lopez Member is found in the Lower Mancos Shale (Fig. 3). The Juana Lopez Member was deposited during the Middle to Upper Turonian during a series of high-frequency transgressive and regressive cycles (Barron et al., 1985; Molenaar, 1983; Fischer et al., 1985; Kauffman, 1985; Nummedal, 1990; Leithold, 1994). The Juana Lopez was deposited within the *Inocermus dimidus* and *Scaphites whitfieldi* biozones (Fig. 3) (Cobban et al., 1994; Joo & Sageman; 2014). These zones lie in the time intervals of *ca* 90.2 myr to *ca* 91.4 myr, encompassing a time interval of *ca* 1.2 myr (Fig. 3).

The Juana Lopez Member is found within the San Juan Basin in New Mexico (Rankin, 1944; Dane et al., 1957; Lamb, 1973; Nummedal & Molenaar, 1995; Ridgley et al., 2013). Rankin (1944) was the first to recognize and name the Juana Lopez Member in the eastern part of the San Juan Basin. The Juana Lopez Member is found above the Dakota Sandstone and the Carlile Member of the Mancos Shale, and below the Upper Gallup Sandstone (Fig. 4) (Dane et al., 1957; Nummedal & Molenaar, 1995; Campbell, 1971; Anderson, 2010; Ridgley et al., 2013). Primary stratigraphic observations describe the Juana Lopez as being predominantly shale interbedded with silt to arenaceous limestone beds in southern New Mexico (Lamb, 1973). Molenaar (1973) describes the Juana Lopez Member as being an organic-rich, mud-dominated shale deposited in a shallow marine offshore environment with low clastic input. Anderson

(2010) interprets the Juana Lopez as being a highly restricted dysoxic to anoxic depositional environment, due to the low diversity microfauna. The Juana Lopez Member is recognized as being organic rich with TOC > 3% and hydrogen index values between 350 and 450, which are much higher than found in the units below and above (Anderson, 2010). Anderson (2010) hypothesizes the depositional controls on the Juana Lopez to be an interaction of tectonics and eustasy.
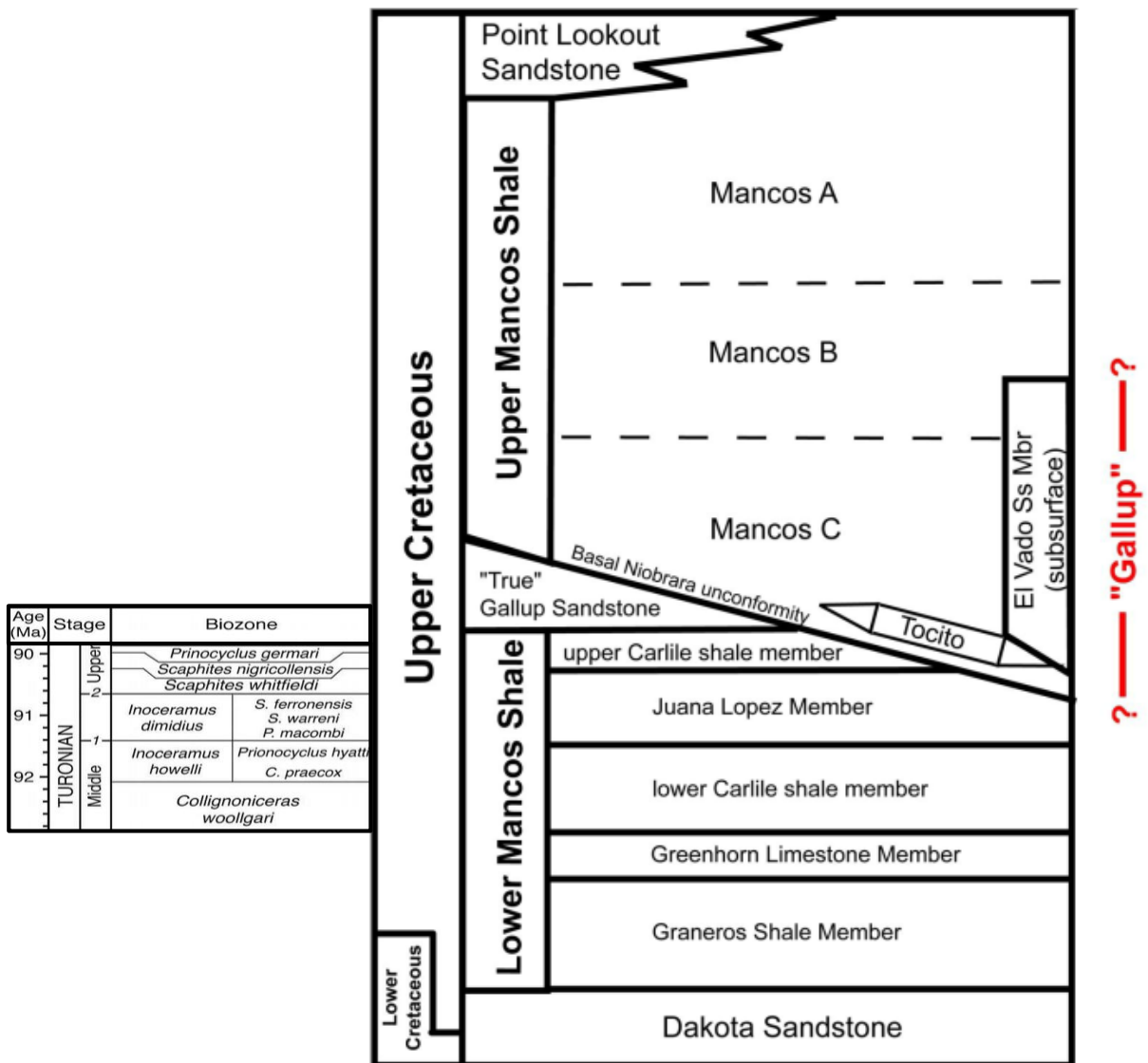
Figure 3- Stratigraphic column of the Mancos Shale with its upper and lower divisions (taken from Broadhead, 2015), with corresponding biozones of the Middle and Upper Turonian (taken from Joo & Sageman, 2014).
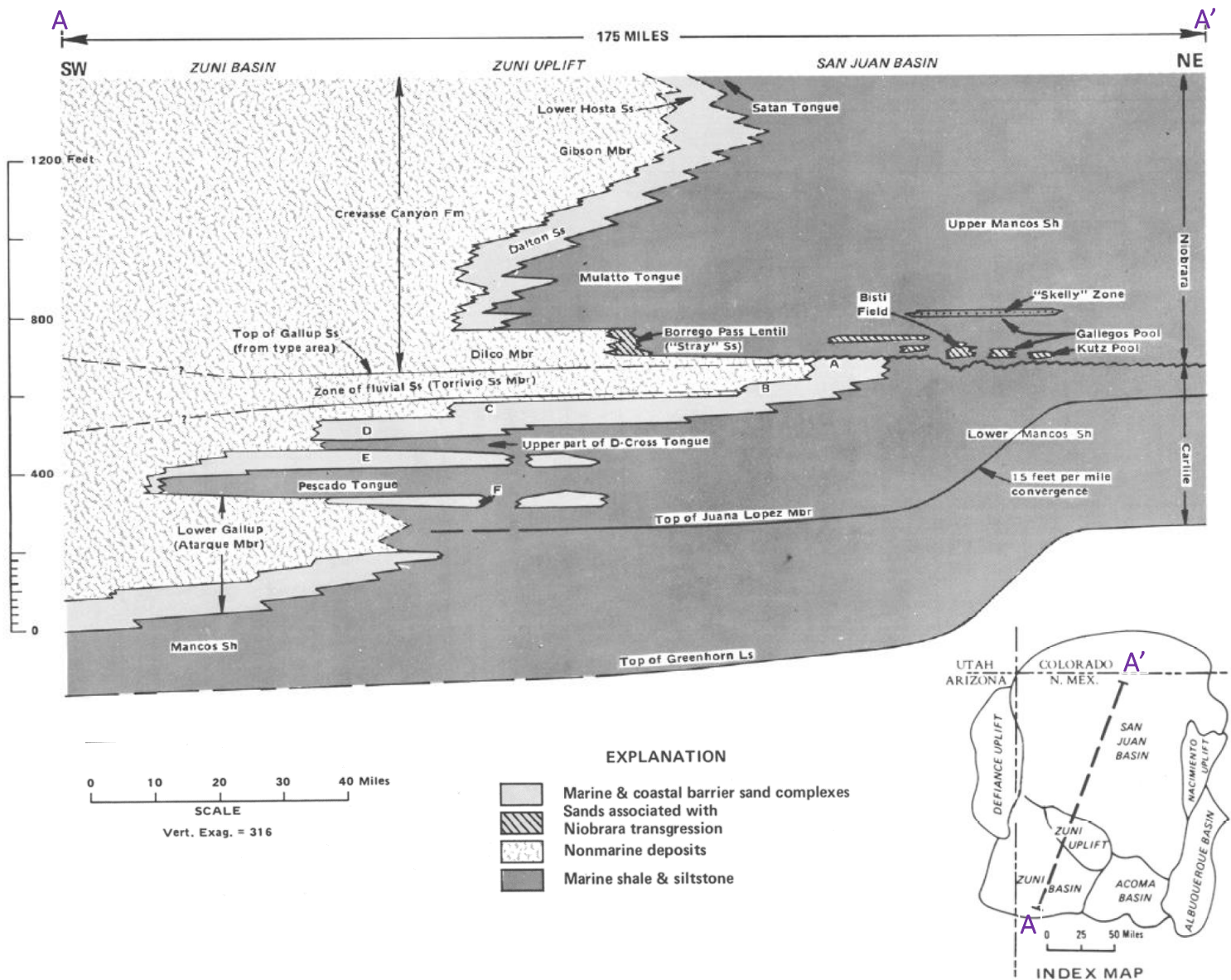
Figure 4- Regional cross section showing showing the stratigraphic top of the Juana Lopez Member to be basinward of the Lower Gallup (Atarque Member) from the Zuni to central San Juan Basin (taken from Molenaar, 1973).

2.1 Study Area

The main study area for this analysis is located west of Shiprock, New Mexico (Fig. 5).

Data for this study was obtained from 10 stratigraphic measured sections (MS1, MS2, MS3A,

MS3B, MS4, MS5, MS6, MS7, MS8A, MS8B) along a north-south trending outcrop exposure of

the Juana Lopez (Fig. 5). Two of the ten sections (MS3B and MS8B) were collected by

8

undergraduate field assistants, Madison MacAndrew and Rachel Nelson, as part of their undergraduate thesis data collection. In addition, one measured section (MS7) was taken just outside of the Mesa Verde National Park in Colorado in a more distal location (shown in Fig. 5A). The Middle to Late Turonian paleoshoreline has been mapped southwest of the study area (Molenaar, 1983), and runs northwest to southeast (Fig. 5). The outcrop exposure is oriented oblique to this paleoshoreline. The distance between the southernmost section (MS3B) and the northernmost section (MS8A) in the New Mexico study area is approximately 47 km (Fig. 5B). The distance between the northernmost section (MS8A) in New Mexico, and the Colorado section (MS7) is approximately 68 km.
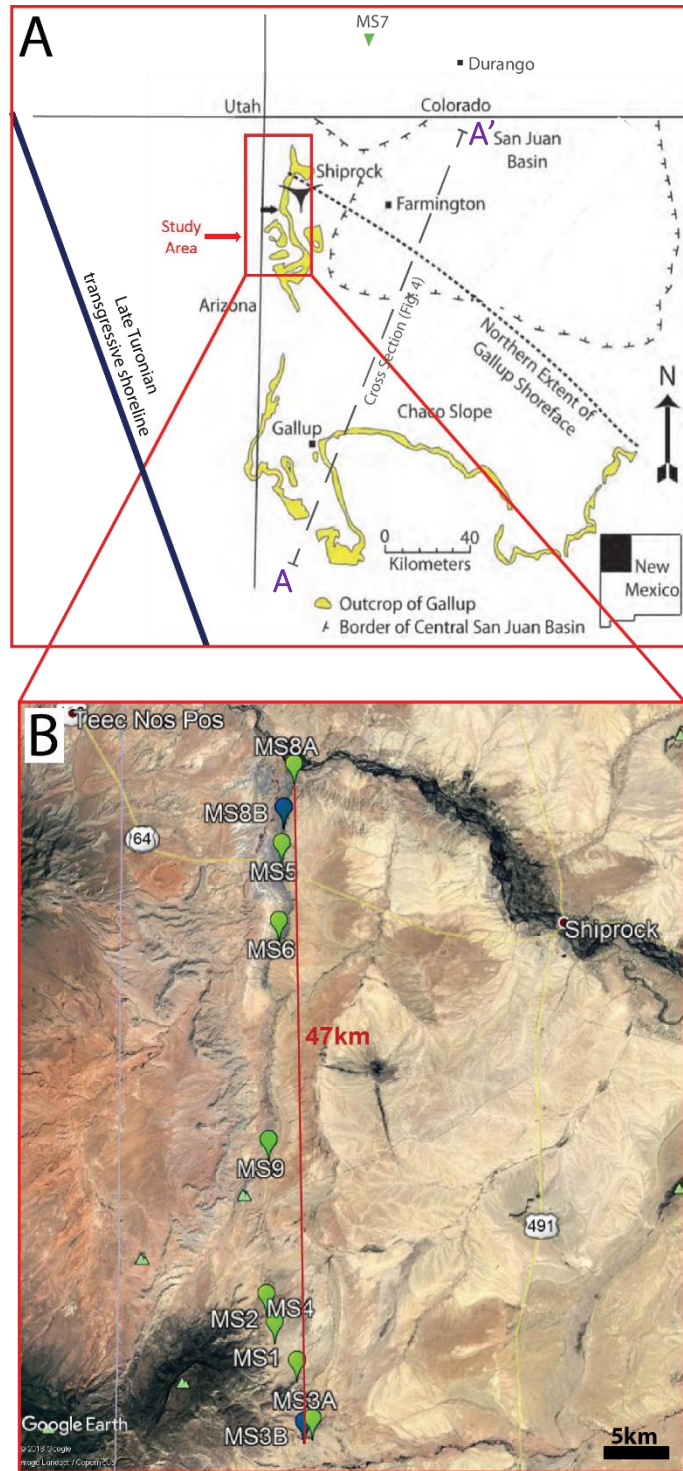
Figure 5- A) Location of the Gallup outcrop belt in the San Juan Basin (modified from Campbell, 1971). The Juana Lopez Member is found directly underlying the Gallup outcrop belt. Location of Colorado measured section (MS7) is shown by a green triangle. Late Turonian transgressive shoreline taken from Molenaar (1983). (B) Locations of ten measured sections west of Shiprock, New Mexico. Blue pins are sections collected by undergraduate students. Red line indicates distance between the two outcrop exposures (47km) (images retrieved from Google Earth).

3. Methodology

The eleven measured sections were measured at centimeter scale. The sedimentological data obtained included, lithology, grain size, sedimentary structures, bed thickness, grading, ichnofacies, degree of bioturbation, fossils and paleocurrents. A bioturbation index of 0 to 6 was used to classify the degree of bioturbation (Fig. 6).

The tools used in the field to collect the data included a Silva Compass for paleocurrent measurements, measuring tape and Jacob's staff for bed thicknesses, hand lens and grain size card for grain size measurements and finally, a hammer and brush for the collection and cleaning of samples and outcrop exposures. The Wentworth classification was used to determine grain size. The percentage of clay content was determined by chewing the rock and through the variation of colour. High percentage of clay content would feel smooth and pasty when chewed, and was mostly dark gray in colour. Low percentage of clay content would feel grittier when chewed, and showed a lighter and browner colour. The upper portion of the Juana Lopez (approximately the top 20 meters) is exposed in outcrop, whereas the lower portion of the member is covered by debris slopes; therefore, a pickaxe was used to excavate trenches to reveal fresh rock for description.

A high-resolution thin-bedded facies analysis was conducted to help determine how the heterolithic units were deposited. The varying depositional processes were identified through the observation of grading patterns, sedimentary structures, bioturbation index and ichnofacies data, allowing the relative proportion of facies association to be calculated. The range of facies proportions are used between MS3A and MS5 in the facies descriptions. A sand-to-shale ratio was determined for each section in the lateral and vertical facies analysis, which shows the proportion of mudstone, heterolithics and sandstone. This classification quantifies the net-to-

gross (N/G) ratio within these sections. The facies proportions used to interpret the relative importance of various sediment delivery and transport processes that can be compared to recent mudstone facies models (e.g. Hart (2016), Schieber (2016), Birgenheier et al. (2017), and Li & Schieber (2018)). A total of 520 paleocurrent measurements were collected and plotted on Rose Diagrams for each section, to interpret the source of sediment feeding the Juana Lopez.

To infer relative sea level fluctuation and to accurately correlate the eleven sections, bentonite layers were used as isochronous datums. Data for both the sections was collected up to 3 meters above a top bentonite layer that lies below the Gallup Sandstone, and in this study is named the "Lower Gallup Bentonite". Where possible, sections were measured into the underlying Carlile Member. The Juana Lopez was differentiated from the Carlile by the appearance of more abundant sandstone laminations. In the study area, the differentiation between the two members was made at a regionally correlated bentonite layer, wherein sandstone laminations are less abundant below the bentonite and more abundant, with increasing thickness, above the bentonite.

Bioturbation Index	Percent Bioturbated	Classification
0	0	No bioturbation
1	1 to 4	Sparse bioturbation, bedding distinct and few discrete traces or escape structures
2	5 to 30	Low bioturbation, bedding distinct, low trace density and escape structures often common
3	31 to 60	Moderate bioturbation, bedding boundaries sharp, traces discrete and overlap rare
4	61 to 90	High bioturbation, bedding boundaries indistinct and high trace density with overlap common
5	91 to 99	Intense bioturbation, bedding completely disturbed (just visible), limited reworking and later burrows discrete
6	100	Complete bioturbation and sediment reworking because of repeated overprinting

Figure 6- Bioturbation index in relation to the percent of sediment that is bioturbated (taken from Gingras et al., 2015, adapted from Taylor & Goldring, 1993).

3.1 <u>Identifying Thin-bedded Depositional Processes</u>

Thin-bedded depositional processes were identified and interpreted based on previously studied facies models of hypopycnal plumes, based on Bates (1953), Lowe (1979), Garvine, (1982), Orton and Reading, (1993), Morehead and Syvitski, (1999), Traykovski et al. (2000), McCool & Parsons (2004), and Schieber (2016), turbidity currents, which include slope failure and hyperpycnal flows, based on Sanders (1960), Bouma (1962), Normark and Piper (1991), Mulder et al. (2003), Friedrichs and Wright (2004), Pattison (2005), Bhattacharya and MacEachern (2009), and Schieber (2016), wave and current enhanced sediment gravity flows, based on Dalrymple et al. (2003), Macquaker et al. (2010), Plint et al. (2012), and Schieber (2016), storm surges, based on Campbell (1966), Harms et al. (1975), Aigner and Reineck (1982), Swift et al. (1983), Seilacher (1984), Duke (1985), Duke et al. (1991), Myrow et al. (2002), and Schieber (2016), and tides, based on Nio and Yang (1991), Dalrymple (2010), and Mackay and Dalrymple (2011).

3.2 <u>Identifying Parasequences and Parasequence Sets</u>

The violation of Walther's Law was used to distinguish parasequences (Walther, 1984; Middleton, 1973). Parasequences are identified by a general coarsening upward facies succession capped by a flooding surface. Flooding surfaces at the top of parasequences were identified by a basinward facies shift, where the most distal facies of the overlying parasequence is found directly above the flooding surface. In this study, and other high-resolution Mancos Shale studies (example the lower Blue Gate Member in the Uinta Basin, Utah from Birgenheier et al., 2017), the thickness and frequency of siltstone and very fine sandstone interlaminations and beds increases upwards within a parasequence, and the clay content decreases upwards (Fig. 7). There is a jump to an increased clay content at the top of the parasequence, indicating a flooding

surface (Fig. 7). Once the parasequences were identified, bentonite layers were used to constrain correlations of parasequences between the eleven sections.

Parasequence sets were identified based on major lap-out, flooding surfaces, as well as observed progradational, aggradational and retrogradational stacking patterns of individual parasequences. A conceptual depiction of the distal expression of sea level change was made through the interpretation of stacking patterns, in combination with facies observations and depositional environment changes.
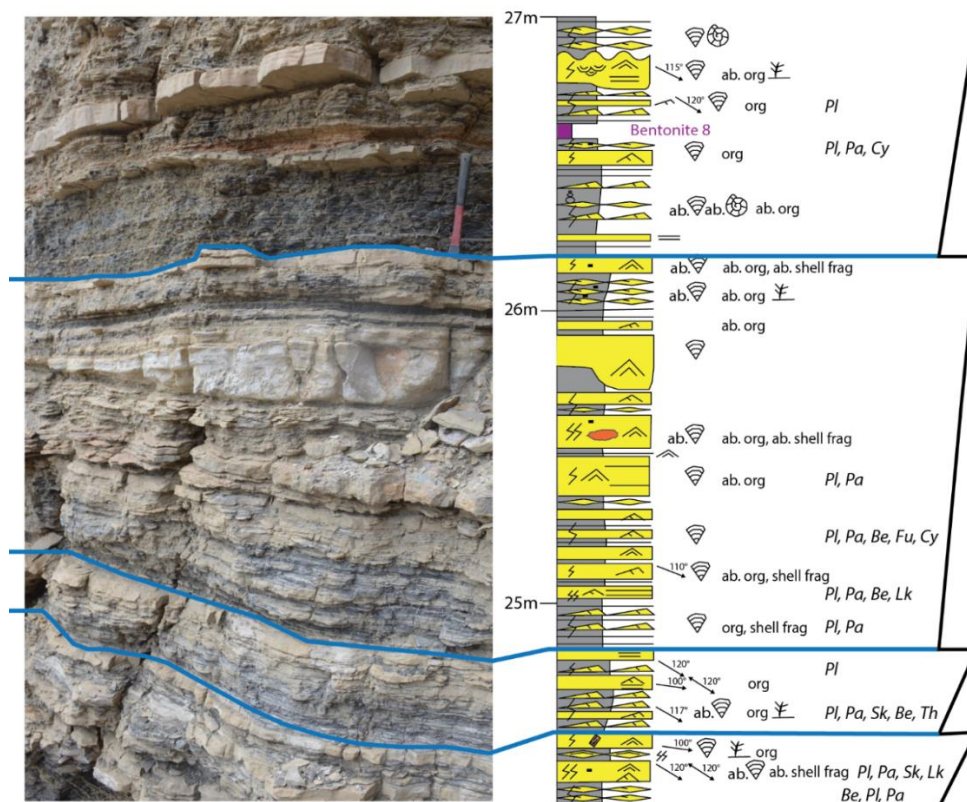
Figure 7- Juana Lopez outcrop exposure at MS3A to the left, and corresponding measured section to the right. Parasequences are identified and flooding surfaces outlined with a blue line. Refer to Figure 22 for a legend associated with the measured section.

4. Facies Description and Interpretation

Facies 1: Bentonite

Bentonite laminae and beds are present in each measured section and throughout the entire Juana Lopez (Fig. 8). Bentonite thickness ranges from 0.1 cm to 40 cm. An average of 10

bentonite layers were found in each measured section. Bentonite layers are identified by their distinctive white to very light grey colour in fresh exposures or orange colour when heavily weathered. Another diagnostic feature is their pasty texture when saturated. The bioturbation in this facies is very low, with BI ranging from 1 to 2. Trace fossils such as *Planolites*, *Palaeophycus* and *Chondrites* are occasionally found at the top of the bentonite layers (Fig. 9A&E). The proportion of this facies ranges from 0.7% to 1.7%.

Interpretation

Bentonites are layers of volcanic ash, which originate from a volcanic eruption (Christidis & Huff, 2009). As volcanic ash is ejected from a volcano, it is transported by wind, tides and currents into offshore marine environments where it then settles across the seafloor (Christidis & Huff, 2009). Therefore, bentonites found in the Juana Lopez are a result of suspension settling of volcanic ash. Due to the ability of volcanic ash to be spread across vast areas of the seafloor, bentonites are used as isochronous datums and used for regional correlation. Trace fossils found in this facies belong to the *Cruziana* ichnofacies indicating an offshore shelf environment in the sublittoral zone of the basin (less than 200 m water depth) (Seilacher, 1967; Frey et al, 1990; Pemberton et al., 1992).
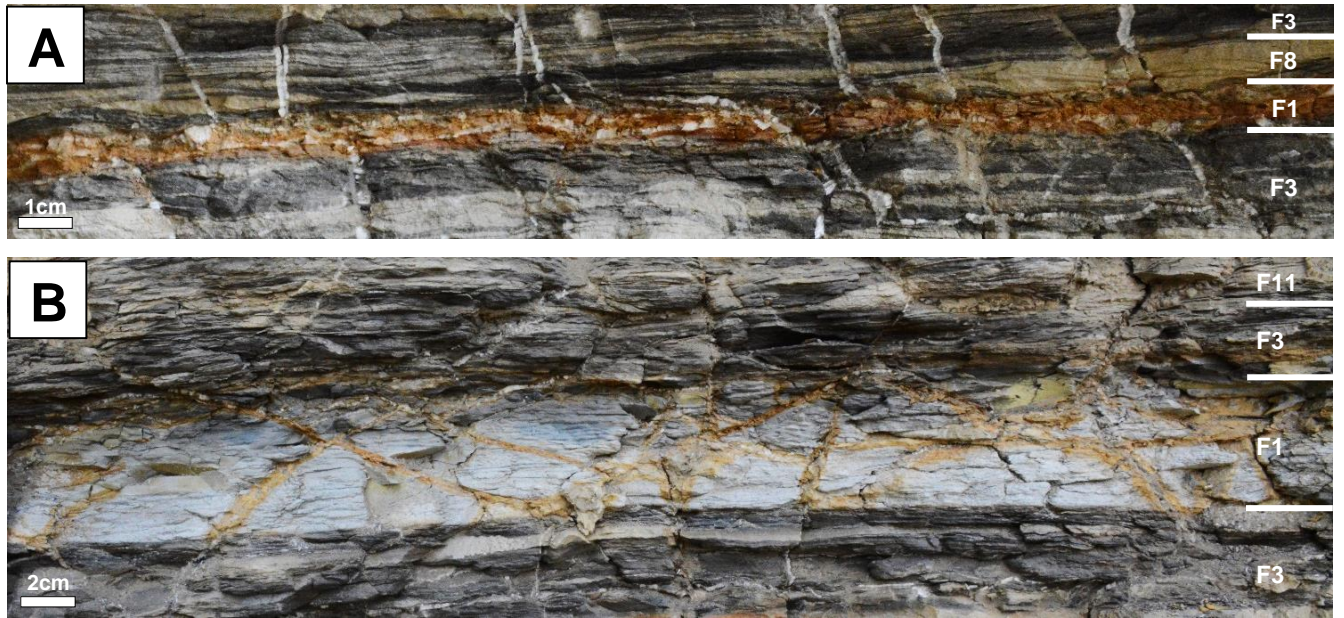
Figure 8- Letter "F" with corresponding numbers represent facies corresponding to the stratigraphy A) F1 showing 2 mm bentonite lamina with a diagnostic orange colour due to weathering B) F1 showing 5 cm bentonite with a diagnostic light grey colour.
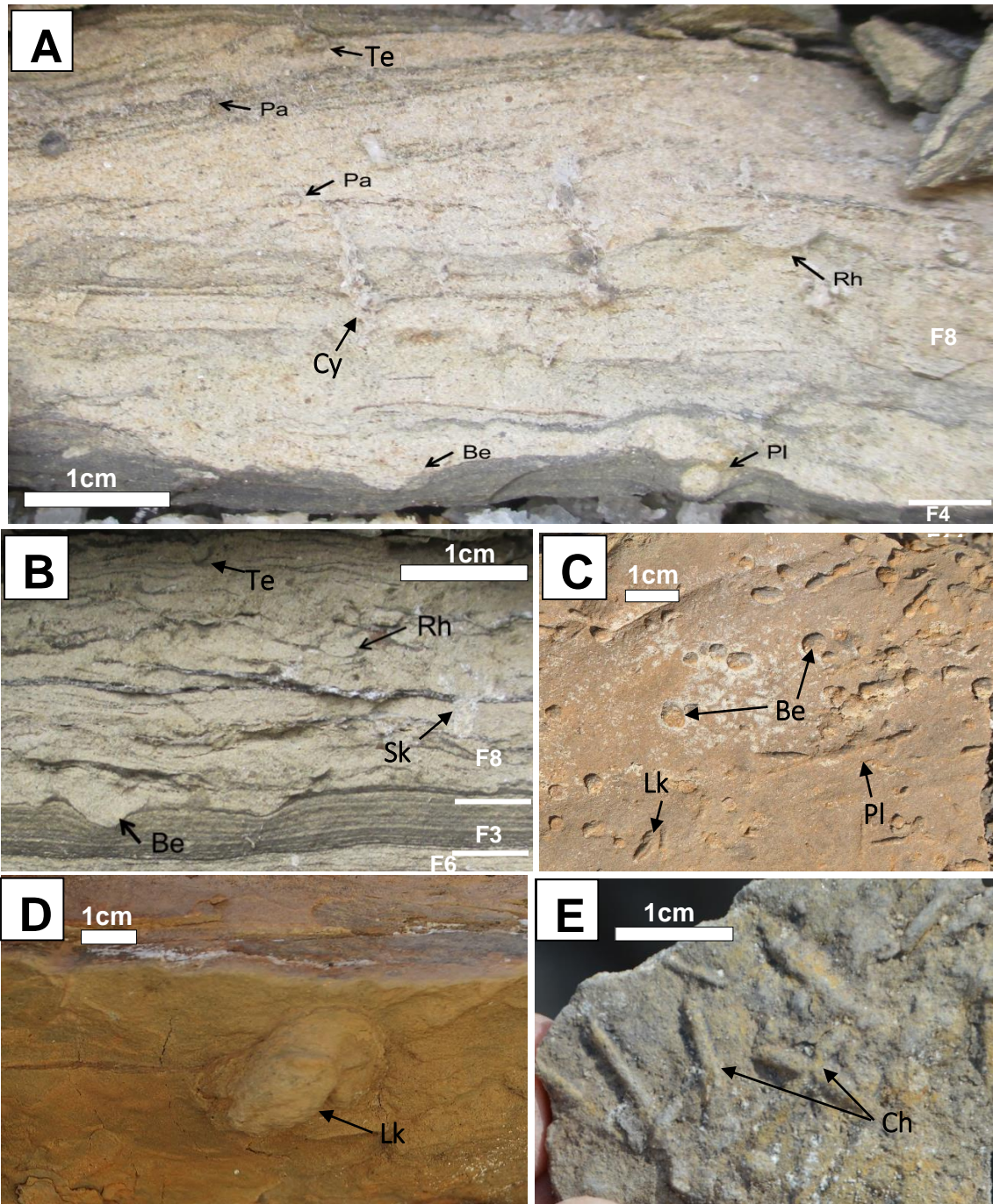
Figure 9- A) Lightly bioturbated current rippled sandstone (F8) (BI = 2) with *Paleophycus* (Pa), *Rhizocorallium* (Rh), *Planolites* (Pl), *Bergaueria* (Be), *Cylindrichnus* (Cy) and *Teichichnus* (Te) trace fossils. B) Moderately bioturbated current rippled sandstone (F8) (BI = 3) with Rh, Be, Te and *Skolithos* (Sk) trace fossils. C) Lightly bioturbated bottom of a wave rippled sandstone bed (F9) (BI = 1) with Be, Pl, and *Lockeia* (Lk) trace fossils. D) Lightly bioturbated bottom of a combined flow rippled sandstone bed (F10) (BI=2) with a Lk trace fossil. E) Lightly bioturbated bottom of a current rippled siltstone bed (F8) (BI = 2) with *Chondrites* (Ch) trace fossils.

Facies 2: Normally Graded

Normally graded beds and laminae are found in each section, except for MS9 (Fig. 10). These strata show an upward reduction in grain size from very fine lower sand to mud. The mud present at the top of the normally graded units has clay contents ranging from 60% to 80%. The graded beds are either structureless, or planar laminated, and lack wave-formed sedimentary structure, such as symmetrical wavy laminations. The thickness of normally graded units range from 0.2 cm to 5 cm. These units contain no bioturbation to very low bioturbation with a BI index of 1. The most abundant trace fossils found in this facies include *Planolites* and *Palaeophycus,* with minor traces of *Cylindrichnus* (Fig. 9A). Shell fragments of inoceramid, ammonite and bivalve fossils can be seen at the base of these units (Fig. 11D). The proportion of this facies ranges from 2.4% to 2.9%.

Interpretation

Normally graded beds record the waning stages of flow, where different sizes of particles settle at different rates (Mulder et al., 2003; Boggs, 2006). As the velocity of flow decreases, coarser grained sediment will settle first, followed by finer and finer grained sediment (Mulder et al., 2001; Mulder et al., 2003). Many of the known mud transport processes form normally graded deposits, and currently it is hard to distinguish the minor differences between the deposits to be able to assign them to specific processes. Normally graded beds can be attributed to ignitive turbidites, hyperpycnites, tempestites, or suspension settling. The lack of wave-formed sedimentary structures and predominance of structureless or planar laminated facies suggests ignitive turbidites, hyperpycnal flows or hypopycnal flows. However, inverse grading was not found in the Juana Lopez, and it is considered unlikely that the inverse grading was eroded from the hyperpycnite deposit throughout the entire Juana Lopez. Therefore, in this study normal

grading of fine-grained sediment is associated as being deposited by low density ignitive turbidites (Normark & Piper, 1991). Trace fossils found in the normally graded units belong to the *Cruziana* ichnofacies found in the proximal to distal offshore shelf (Seilacher, 1967; Frey et al, 1990; Pemberton et al., 1992). The very low to non-existent BI, as well as the disaggregated shell fragments, indicates high sedimentation rates and a low infaunal biomass (Gingras et al., 2015), consistent with high depositional rates from waning turbidity currents.

Figure 10- Normally graded laminae showing very fine lower sandstone transitioning upwards to mudstone with 75% clay content.
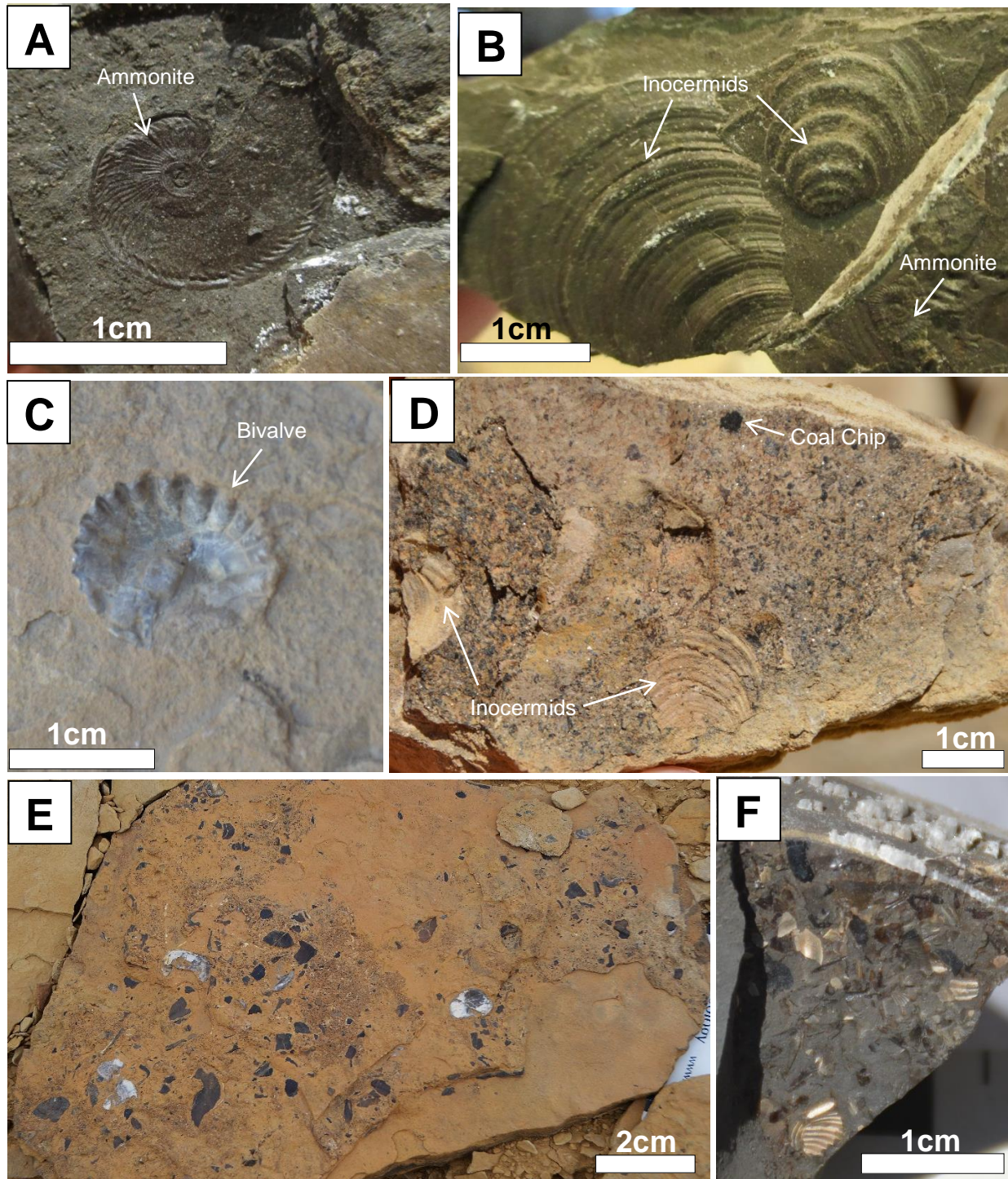
Figure 11- A) Ammonite fossil preserved in shaly claystone (F4). B) Inoceramid and ammonite fossils preserved in planar interlaminated mudstone and sandstone (F3). C) Bivalve fossil found in a combined flow rippled sandstone (F10). D) Shell fragments, inoceramid fragments, coal chips and organic matter found in a planar laminated sandstone bed (F6). E) Disaggregated shell fragments (mostly of inocermids) typically found in the top rippled sandstones of the Juana Lopez. F) Disaggregated shell fragments found in a siltstone starved ripple (F11).

Facies 3: Planar Interlaminated Mudstone and Sandstone

This facies consists of rhythmic planar interlaminations of clays and silts with very fine lower sands (Fig. 12). In a 2.1 cm sample of this facies, 31 very fine lower sandstone laminations were found with interlaminated homogeneous and structureless mudstone (Fig. 12). Interlaminated units range in thickness from 0.5 cm to 80 cm, and show no bioturbation to low bioturbation with a BI index of up to 2. Trace fossils found in these units include *Planolites*, *Palaeophycus, Thalassinoides*, *Phycosiphon*, *Bergauria*, *Rhizocorallium* and *Fugichnia*, with *Planolites*, *Palaeophycus* and *Bergauria* being the most abundant (Fig. 9A&B). Small scale shell fragments are occasionally found in the sandstone laminations and mudstone laminations (Fig. 11D&F), whereas fully preserved inoceramid and ammonite fossils are occasionally found in the mudstone laminations (Fig. 11A&B). This facies comprises the largest proportion of the Juana Lopez sections, with proportions ranging from 26.0% to 42.1%.

Interpretation

The rhythmic pattern of alternating sand and mud likely represent tidal laminites, which typically represent a single tidal cycle (Dalrymple, 2010). The planar laminations found in tidal laminites are deposited from suspension, where sand is deposited when current speeds are the highest (during the middle of each ebb and flow tide) (Nio &Yang, 1991; Dalrymple, 2010). Fluid muds tend to lack bioturbation, grading and internal laminations (Dalrymple et al., 2003). Recent studies have confirmed that, unlike passively deposited mud drapes, dynamically deposited fluidized mud flows are also found in tidal deposits (Mackay & Dalrymple, 2011). This facies is associated with tidal currents and fluid muds. Tides are interpreted to transport sediment further offshore along with near bed currents formed by waves maintaining a traveling layer of fluid mud, which can transport muds up to 400 km offshore (Bhattacharya &

MacEachern, 2009; Mackay & Dalrymple, 2011; Schieber, 2016). Trace fossils found in this facies belong to the *Skolithos* and *Cruziana* ichnofacies (Seilacher, 1967; Frey et al, 1990; Pemberton et al., 1992). *Skolithos* can be formed by many different types of organisms and is therefore found in virtually every type of marine depositional environment; however, *Cruziana* is mostly found in the proximal to distal offshore shelf (Pemberton et al., 1992). The very low BI indicates high sedimentation rates (MacEachern et al., 2005; Hovikoski et al., 2008; Gingras et al., 2015). Shell fragments found in the sandstone laminations would have been transported and reworked during the middle of each ebb and flow tide, where energy increases and current speeds are the highest (Nio &Yang, 1991; Dalrymple, 2010).
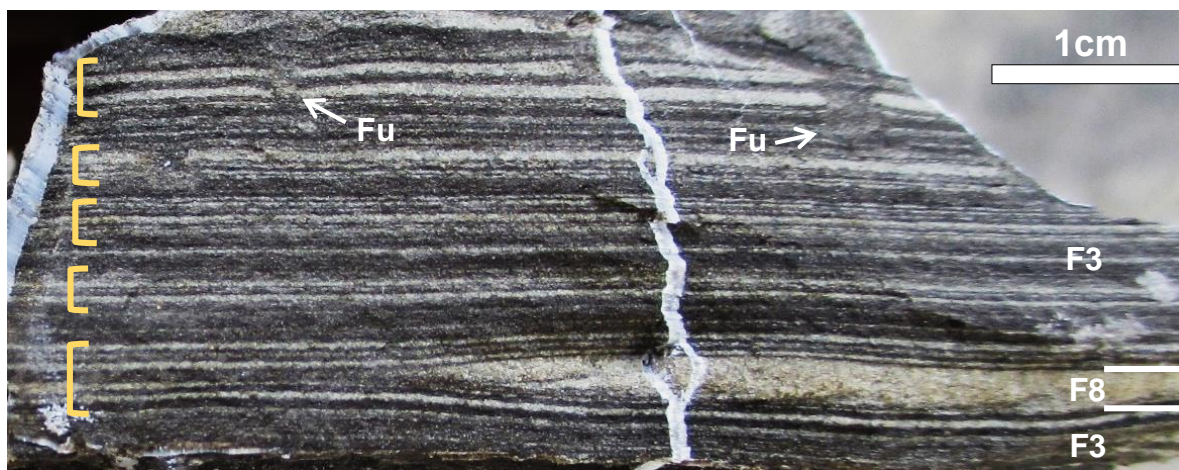
Figure 12- Planar interlaminated mudstone and sandstone in MS2 (F3) with a small starved current rippled sandstone lamina (F8) and a BI of 1. *Fugichnia* (Fu) burrow shown in F3. Possible spring cycles are outlined within yellow bracketed packages on the left, and in between are possible neap cycles.

Facies 4: Shaly Claystone

Shaly claystone is the one of the most abundant facies found in all the sections (Fig. 13). This facies consists of fissile units of clay sized particles with 50% to 90% clay content. Clean cut rows of the shaly claystone show no structure, however, thin sections may show otherwise. These shale units range in thickness from 0.1 cm to 50 cm and have a BI of 0 to 1 in all sections, showing traces of *Planolites* (Fig. 9A). Very well preserved fossils of ammonites, inoceramids

and fish scales can be found in this facies (Fig. 11A&B). The proportion of this facies ranges from 17.1% to 25.0%.

Interpretation

Shaly claystone is likely the result of suspension settling of aggregated clay particles from buoyant plumes (McCool & Parsons, 2004; Boggs, 2006). In this study, shaly claystone is given a suspension settling association, since aggregated clay particles are assumed to be transported offshore from along-shelf current buoyant plumes. Very low to non-existent BI in facies 4, found within the *Cruziana* ichnofacies, indicates high sedimentation rates with suspended settling onto a distal offshore shelf (Pemberton et al., 1992; MacEachern et al., 2005; Hovikoski et al., 2008; Gingras et al., 2015).
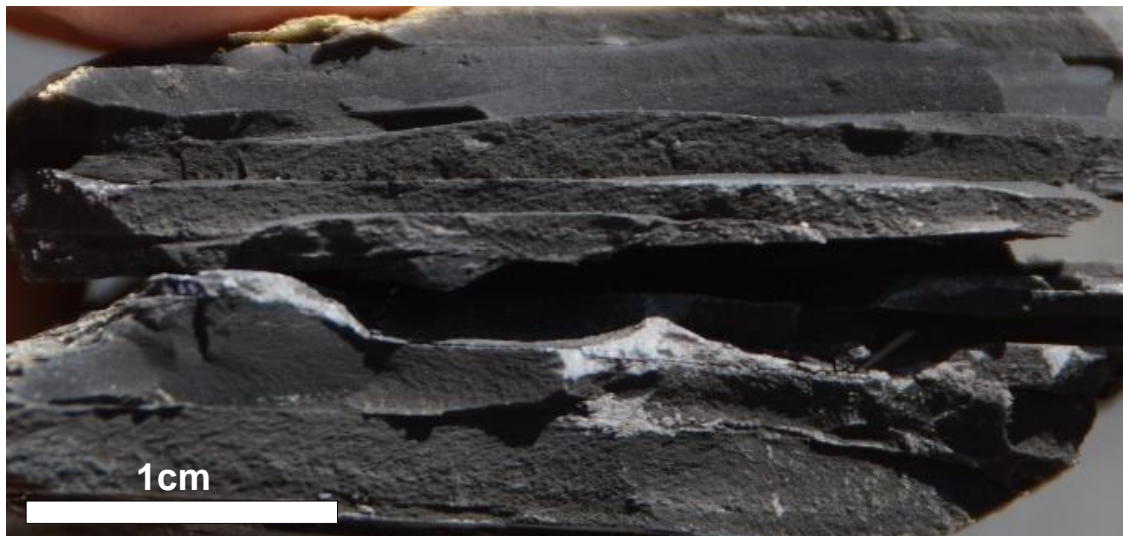
Figure 13- Black shaly claystone displaying fissile nature and homogeneous texture.

Facies 5: Micro-hummocky Cross-stratified Sandstone

Micro-hummocky cross-stratified sandstone is found in the upper Juana Lopez sandstone units (Fig. 14). This facies consists of very fine lower to very fine upper sandstone with a sharp erosional base. Wavelength of bedforms ranges from 10 cm to 25 cm. The thickness of this facies ranges from 10 cm to 40 cm. The wavelength of micro-hummocks is differentiated from

the wave rippled siltstone and sandstone facies (F9) by the larger scale. This facies shows light to moderate bioturbation, with a BI ranging between 0 and 3. A diversity of trace fossils is found in this facies, including *Planolites, Palaeophycus*, *Thalassinoides, Lockeia*, *Bergaueria, Cylindruchnus, Skolithos,* and *Rhizocorallium*. However, *Skolithos, Lockeia* and *Bergaueria* are most common (Fig. 9C&D). Disaggregated shell fragments of larger scale inoceramids and ammonites are commonly found in this facies, as well as organic matter (including coal chips and wood chips) (Fig. 11E). The proportion of this facies ranges from 0.7% to 1.2%.

Interpretation

Micro-hummocky cross-stratification shows evidence of oscillatory flow. Above storm wave base, strong storm-wave surges transport coastal sediment to the shelf under oscillatory-dominant combined flows forming tempestite deposits (Duke et al., 1991; Aigner & Reineck, 1982). These combined-flows are produced by along-shelf geostrophic flows (Swift et al., 1983). *Skolithos* ichnofacies (suggested by the most common trace fossils) and the abundant shell fragments and organics, in conjunction with the interpretation of deposition above storm wave base, suggest the depositional environment to be in a proximal offshore shelf (Frey et al, 1990; Pemberton et al., 1992).
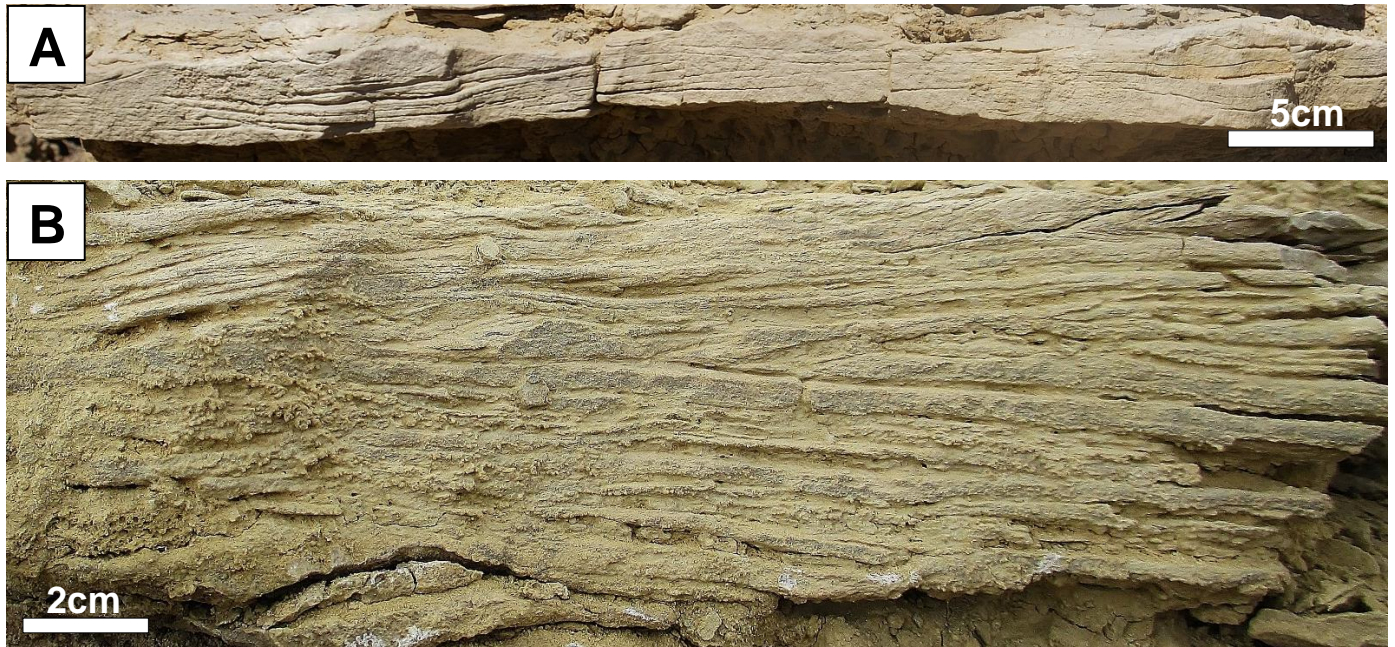
Figure 14- Micro-hummocky cross-stratified sandstone. A) Large wavelength ripples are seen that have a length of 20 cm. B) Larger scale undulating ripples.

Facies 6: Planar Laminated Siltstone and Sandstone

This facies consists of planar laminated beds of siltstone with 5% to 45% clay content to very fine lower sandstone (Fig. 15). Laminations appear planar, however certain units appear to have some gentle undulation, representing quasi-planar lamination (Arnott, 1993). These deposits have an erosional base, where tool marks and scours are also found (Fig. 16). Units range in thickness from 3 cm to 28 cm and have a low BI of 0 to 2, showing traces of *Planolites, Phycosiphon* and *Bergauria* (Fig. 9C). Shell fragments of inoceramids and ammonites, as well as organics are common in this facies (Fig. 11D&E). The proportion of this facies ranges from 1.9% to 2.4%.

Interpretation

Planar laminated siltstone and sandstone can be interpreted as either the result of high flow velocities washing out the formation of ripples as the formation of flow separation is suppressed at higher velocites, or as the result of suspension settling of fine-grained silt and sand

particles from buoyant plumes (Boggs 2006; Nichols, 2009). Quasi-planar lamination is

hypothesized to be produced by high-energy combined flows (Arnott, 1993). The presence of

tool marks and scours at the erosional base of these deposits indicate deposition by high velocity

unidirectional currents, suggesting wave modified turbidity currents. Low BI indicates rapid

settling rates (MacEachern et al., 2005; Hovikoski et al., 2008; Gingras et al., 2015). Trace

fossils suggest a *Cruziana* and *Skolithos* ichnofacies indicating a proximal to distal offshore shelf

environment (Seilacher, 1967; Frey et al, 1990; Pemberton et al., 1992). Shells would be

disaggregated and reworked when transported by wave modified turbidity currents onto the

proximal to distal shelf.

Figure 15- A) Quasi-planar laminated silstone with 20% clay content showing subtle undulation. B) Planar laminated very fine lower sandstone.

Figure 16 – Tool marks and scours at the erosional base of a planar laminated very fine lower sandstone bed. Blue arrow indicates general flow direction.

Facies 7: Structureless Siltstone and Sandstone

Structureless siltstone and sandstone units consist of silt sized particles with 5% to 45% clay content to very fine lower sand sized particles that appear homogeneous and lack internal sedimentary structures (Fig. 17). The structureless siltstones and sandstones have an erosional base. These units range from 0.2 cm to 15 cm. There is little to no evidence of bioturbation, with a maximum BI of 1, with rare *Planolites*. Occasionally, small scale disaggregated shell fragments are found. The proportion of this facies ranges from 0.2% to 0.4%.

Interpretation

Similar to facies 4, the lack of internal structures and bioturbation in facies 7 indicates very rapid deposition of silt to sand sized sediment formed from suspension (Boggs, 2006; Macquaker et al., 2010). This facies could have also been deposited from a very highly concentrated sediment dispersion during sediment gravity flows, suggesting an ignitive turbidite deposit (Boggs, 2006; Macquaker et al., 2010). The lack of structure and erosional base may represent the base of a Bouma Sequence. The very low to non-existent BI in this facies suggest

27

very rapid sedimentation rates (MacEachern et al., 2005; Hovikoski et al., 2008; Gingras et al., 2015).
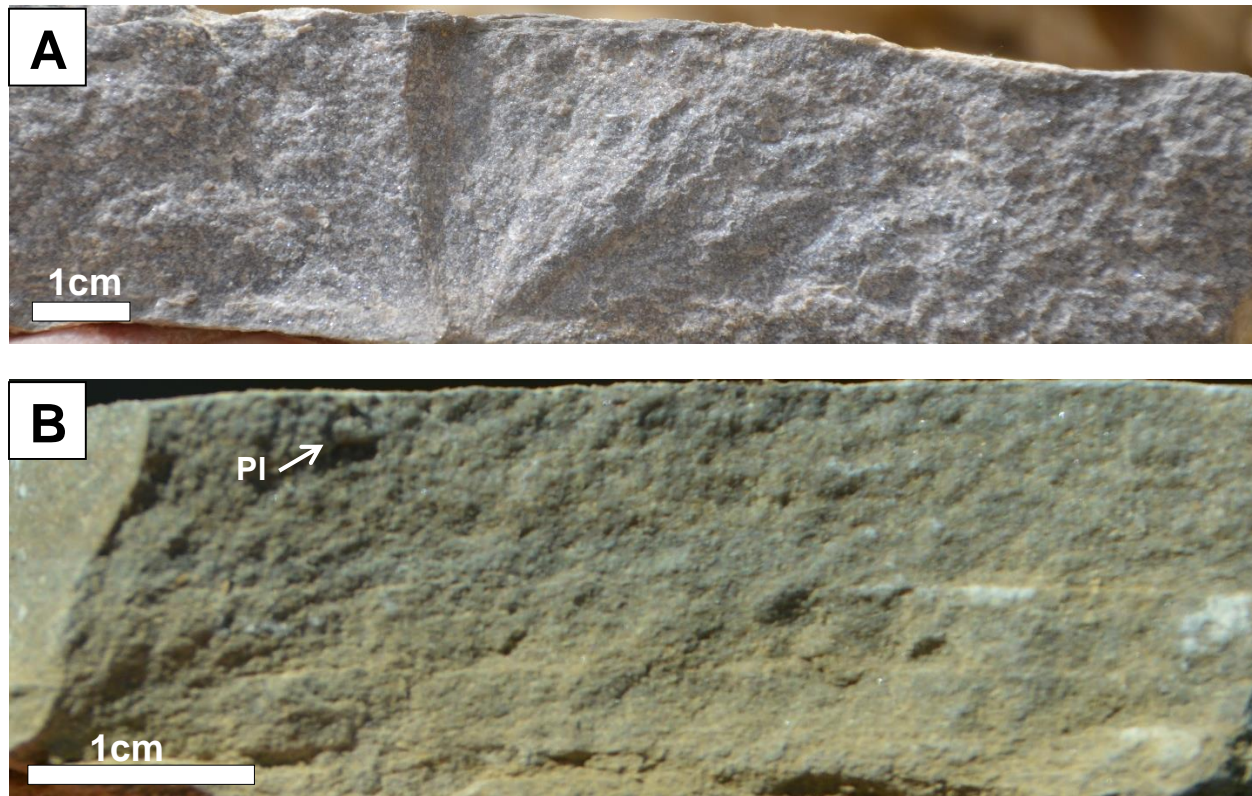
Figure 17- A) Stuctureless siltstone with 15% clay content. B) Structureless very fine lower sandstone with a *Planolites* (Pl) burrow.

Facies 8: Current Rippled Siltstone and Sandstone

Current rippled siltstone and sandstone is found in all sections and consists of units with silt to very fine lower sand grains, showing evidence of unidirectional ripple laminations with a typical NW flow direction (Fig. 18). This facies is also seen as starved current rippled siltstone and sandstone units. The thickness of these units ranges from 0.3 cm to 35 cm. This facies shows a variety of lightly bioturbated to moderately bioturbated units with BI ranging from 0 to 3. Trace fossils include *Planolites, Palaeophycus*, *Thalassinoides, Lockeia*, *Bergaueria, Skolithos*, and *Rhizocorallium* (Fig. 9A-D). The most abundant trace fossils are *Planolites, Palaeophycus,*

Lockeia and *Bergaueria*. Shell fragments of inoceramids, ammonites and bivalves, as well as organics are common. The proportion of this facies ranges from 4.0% to 8.0%.

Interpretation

Current rippled laminations form as the result of unidirectional flow and are distinctly asymmetrical (Allen, 1969; Nichols, 2009). Current ripples are common in the T_C division of the Bouma sequence, suggesting deposition by ignitive turbidity currents. Storms with strong unidirectional flow components are also capable of forming unidirectional ripple laminations, but these will typically show reworking by waves. Along-shelf geostrophic and ocean currents may also result in the formation of current ripples (Schieber, 2016). Contourites are formed by the contour-parallel current enhanced sediment gravity flows that are reworked by the persistent action of bottom currents, and also show evidence of current rippled lamination (Stow et al., 2002; Rebesco et al., 2014). Low to moderate BI indicate rapid to moderate sedimentation rates (MacEachern et al., 2005; Hovikoski et al., 2008; Gingras et al., 2015). The majority of the trace fossils are found in the *Skolithos* ichnofacies and suggest the depositional environment to be in the proximal offshore shelf (Frey et al, 1990; Pemberton et al., 1992). Shells are transported from the proximal shelf and are reworked and disaggregated by the time they are deposited.

Figure 18- A) Current rippled siltstone with an overlying structureless siltstone bed (F7), fluid mud lamination (F4) and planar laminated siltstone bed (F6). B) Current rippled very fine lower sandstone bed.

Facies 9: Wave Rippled Siltstone and Sandstone

Wave rippled siltstone to very fine upper sandstone is present in all sections (Fig. 19). Paleocurrents show a predominant NW-SE flow direction. The wavelength of the ripples are smaller than those of the micro-hummocky cross stratified ripples (F5), and range from 1 cm to 10 cm. The base of these deposits are sharp and erosional. The thickness of this facies ranges from 0.3 cm to 80 cm, and is also seen as starved rippled siltstone and sandstone units. This facies shows light to moderate bioturbation with a BI ranging between 0 and 3. Trace fossils include *Planolites, Palaeophycus*, *Thalassinoides, Lockeia*, *Bergaueria, Cylindruchnus, Skolithos,* and *Rhizocorallium*. Larger scale, intact, and disaggregated pieces of inoceramids, ammonites and bivalves are very common (Fig. 11E). The proportion of this facies ranges from 6.0% to 19.2%.

Interpretation

Wave-ripple laminations consists of parallel laminae that conform to the surface form of a wave ripple and are formed as a result of oscillatory flow (Campbell, 1966). These wave ripple laminations are likely caused by storm-generated waves and are therefore interpreted as tempestites caused by storm surges (Harms et al., 1975; Aigner 1982; Duke, 1985; Myrow et al., 2002). The presence of starved wave rippled siltstone and sandstone units indicates strong flow caused by storm surges, with limited sediment supply (Kane et al., 2007; Nichols, 2009). Low to moderate BI indicate rapid to moderate sedimentation rates (MacEachern et al., 2005; Hovikoski et al., 2008; Gingras et al., 2015). The majority of the trace fossils are from the *Skolithos* ichnofacies, interpreted to be found in a proximal offshore shelf (Frey et al, 1990; Pemberton et al., 1992). Storms are capable of transporting larger scale shells to the offshore, where storm-generated waves would break them apart prior to their final deposition.

Figure 19- A) Wave rippled siltstone with 10% clay content and a wavelength of 6 cm. B) Wave rippled very fine lower sandstone.

Facies 10: Combined Flow Rippled Siltstone and Sandstone

Combined flow rippled siltstone to very fine upper sandstone is found in all sections and consists of units with silt to very fine upper sand sized grains (Fig. 20). Flow directions for current rippled laminations are typically NW and flow directions for wave rippled laminations are typically NW-SE (i.e. perpendicular to wave ripple crests). The thickness of these units range from 1 cm to 1.75 m. This facies is lightly to moderately bioturbated, with a BI range of 0 to 3. There are a variety of trace fossils in this facies, such as *Planolites, Palaeophycus, Cylindrichnus, Rhizocorallium, Skolithos, Thalassinoides*, *Bergaueria,* and *Lockeia*, and rare *Teichichnus*. Larger scale, fully preserved, and disaggregated pieces of inoceramids, ammonites and bivalves, as well as organics, are very common (Fig. 11E). The proportion of this facies ranges from 9.2% to 21.2%

Interpretation

Combined flow rippled laminations are a result of the action of both waves and currents (Nichols, 2009). This facies is likely the result of wave-modified tempestites, or wave-modified turbidites, which include oscillatory and density-induced flows (Duke, 1985; Myrow et al., 2002). This process occurs when a current is generated by a storm surge at the same time as high-amplitude waves reach deep below the surface (Nichols, 2009). Therefore, this facies is classified as a wave modified turbidite/tempestite.

Figure 20- Very fine lower combined flow rippled sandstone showing both current and oscillatory flow.

Facies 11: Starved Rippled Siltstone and Sandstone

The starved rippled siltstone and sandstone facies consists of lenticular silt to very fine lower sand beds with undefined ripple laminations, as shown in Figure 21. This facies was present in all sections with thicknesses ranging from 0.1 cm to 6 cm. This facies is lightly bioturbated with a BI ranging from 1 to 2. These units have *Planolites, Palaeophycus, Bergaueria*, *Lockeia* and *Rhizocorallium*. Small scale shell fragments are occasionally found. The proportion of this facies ranges from 1.1% to 5.0%.

Interpretation

Starved siltstone/sandstone ripples indicate limited sediment availability, which was driven by unidirectional or oscillatory flows (turbidity currents or storm surges) and draped by suspended mud sized particles when flow energy waned (Kane et al., 2007). Since the type of ripples are unrecognizable in these facies, the exact origin cannot be unequivocally determined.
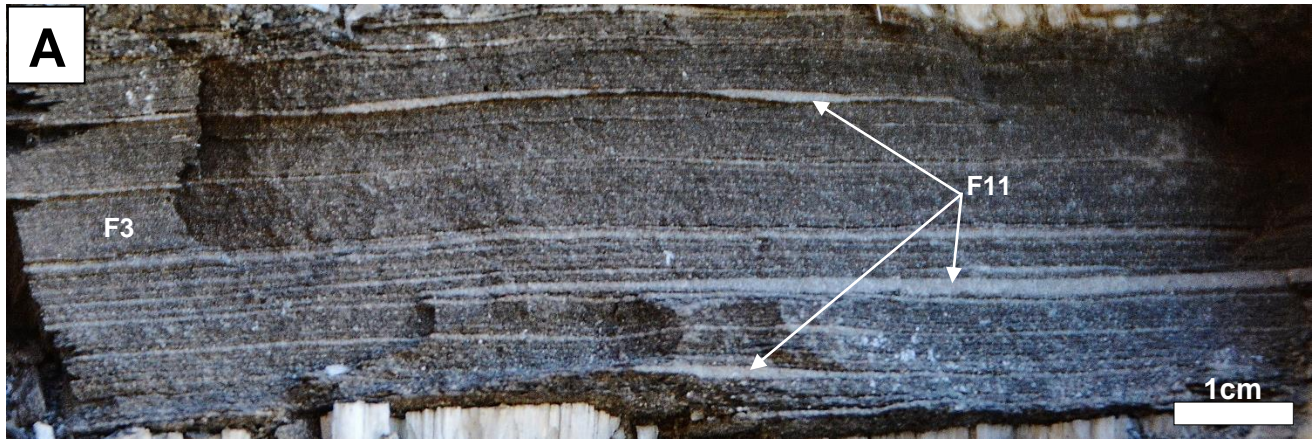
Figure 21- A) Starved rippled siltstone laminations within a planar interlaminated mudstone and sandstone unit. (B) Starved rippled sandstone bed (F11) with an observed external asymmetric current ripple and no internal features, surrounded by planar interlaminated mudstone and sandstone (F3).

5. Vertical and Lateral Facies Variability

Measured sections are between 22 to 56 meters thick. The thickness of the entire Juana Lopez, in the sections where it was possible to measure (MS3A and MS3B), ranges from 37 to 43 meters. A legend and facies key associated with the measured sections and facies analysis is shown in Figure 22.

Vertical Facies Analysis

A vertical facies analysis was conducted between a proximal section (MS3B) containing the complete Juana Lopez stratigraphy, and a distal section (MS5) containing the most complete

distal Juana Lopez stratigraphy (Fig. 23). The vertical facies analysis is divided into 3 portions; (1) the Carlile Shale, (2) the lower Juana Lopez and (3) the upper Juana Lopez. Table 1 shows the percentages of each facies in each of the 3 portions, as well as the facies associations corresponding to each facies. The resulting percentages of depositional processes in each portion are recorded in Table 2. For the sand-to-shale analysis, the mudstone facies association is made up of F4, the heterolithics facies association is made up of F2 and F3, and the sandstone facies association is made up of F5, F6, F7, F8, F9, F10 and F11.

The dominant facies in the Carlile Shale include shaly claystone (F4) and planar interlaminated mudstone and sandstone (F3), resulting in the highest proportion of depositional processes to be suspension settling and fluid muds/tidal currents. The sand-to-shale ratios are dominated by mudstones.

Similar to the Carlile Shale, the dominant facies in the lower Juana Lopez include shaly claystone (F4) and planar interlaminated mudstones and sandstones (F3); however, the percentage of rippled siltstone and sandstone (F8, F9 and F10) increases noticeably in the lower Juana Lopez. Planar interlaminated mudstones and sandstones facies (F3) are most abundant in the lower Juana Lopez portion, making the sand-to-shale ratios to be dominated by heterolithic reservoirs, and indicating fluid muds/tidal currents to be the dominant depositional process. In addition, an increase in tempestites, ignitive turbidites and wave modified turbidites/tempestites is also observed.

The upper Juana Lopez has a noticeable decrease in shaly claystone (F4) and planar interlaminated mudstones and sandstones (F3), with wave and combined flow rippled sandstones (F9 and F10) being the most abundant. Micro-hummocky cross stratified sandstone is only found in the upper Juana Lopez portion, suggesting a transition to a higher energy storm influenced

35

environment, where waves from storm surges have a stronger ability to rework the sediment on the seafloor. With rippled siltstones and sandstones being the most abundant in the upper Juana Lopez, tempestite, ignitive turbidite and wave modified turbidite/tempestite are the dominant depositional processes. The sand-to-shale ratios are dominated by sandstone reservoirs, making the upper Juana Lopez a sandstone-dominated unit.

Moving vertically up the stratigraphic section from the Carlile to the lower to upper Juana Lopez, the percentage of siltstone and sandstone facies increases, and the sand-to-shale ratios go from mudstone-dominated to heterolithics-dominated to sandstone-dominated, respectively. These trends suggest an overall shoaling and regressive environment. BI generally decreases from the lower to upper Juana Lopez, whereas disaggregated shell fragments increase in rippled siltstones and sandstones, suggesting increasing energy, sedimentation rate and dynamically deposited sedimentary structures.

Lateral Facies Analysis

A lateral facies analysis was conducted within the middle portion of the Juana Lopez, which correlated across the entire study area (outlined in Fig. 24). This stratigraphic interval was defined between a bentonite (at the base) and a flooding surface (at the top). The bentonite layer thickens northward from 1 cm to 30 cm. The flooding surface is found on top of a sandstone bedset package exhibiting wave to micro-hummocky cross stratification (F9 and F5). Table 3 shows the percentages of each facies in each individual measured section arranged from south to north, as well as the depositional processes corresponding to each facies. The resulting percentages of depositional processes are recorded in Table 4.

The percentage of rippled siltstone and sandstone facies (F5, F8, F9 and F10) decreases from south (MS3A) to north (MS7), whereas the percentage of planar interlaminated mudstones

and sandstones (F3) increases (also shown in Fig. 23 between MS3A and MS5). This results in sandstone reservoirs in the sand-to-shale ratios to be decreasing northward, and heterolithic reservoirs to be increasing. This is due to the increasing distance away from the shoreline, where sandstone dominated bedsets pinch-out into laminae. This trend results in a systematic increases in fluid muds/tidal currents to the north, with the highest proportion shown in the distal MS7 Colorado section.

MS1, MS2 and MS4 have the highest proportions of turbidites, due to the increase in normal grading (F2) and current rippled siltstones and sandstones (F8). This observation suggests proximity to a delta source in this area. The proportion of wave rippled siltstones and sandstones (F9) increase northward of MS4 and southward of MS1, away from the delta source. This results in tempestite and wave modified turbidites/tempestites to increase southward and northward from the possible delta source area. Li et al. (2015) shows similar observations in parasequence 6 of the middle Turonian Tununk Member underlying the Ferron Sandstone in Utah. Parasequence 6 in the Tununk displays a wave-dominated environment to the north passing abruptly into a fluvial-dominated, wave-influenced environment southward and back to a wave-dominated environment further south (Li et al., 2015). These observations lead to the interpretation of a storm-dominated symmetrical delta with a large river-dominated bayhead system (Li et al., 2015).

Facies

1. Bentonite
2. Normally Graded
3. Planar Interlaminated Mudstone and Sandstone
4. Shaly Claystone
5. Micro-hummocky Cross-stratified Sandstone
6. Planar Laminated Siltstone and Sandstone
7. Structureless Siltstone and Sandstone
8. Current Rippled Siltstone and Sandstone
9. Wave Rippled Siltstone and Sandstone
10. Combined Flow Rippled Siltstone and Sandstone
11. Starved Rippled Siltstone and Sandstone

Facies Associations

Suspension Settling
Fluid Muds/Tidal Currents
Ignitive Turbidite
Tempestite
Wave Modified Turbidite/Tempestite
Unknown

Sedimentary Structures

Current Rippled Lamination
Wave Rippled Lamination
Combined Flow Rippled Lamination
Planar Lamination
Micro-Hummocky Cross Stratification
Starved Rippled Lamination
Starved Current Rippled Lamination
Starved Wave Rippled Lamination
Starved Combined Flow Rippled Lamination
Lightly Bioturbated (BI = 1 - 2)
Moderately Bioturbated (BI = 3 - 4)
Soft Sediment Deformation
Normally Graded
Calcareous Nodule
Coal Chips
Wood Chips
Plant Material
Cone-in-cone

Lithology

Claystone
Siltstone
Sandstone
Bentonite

N/G

Mudstone
Heterolithics
Sandstone

Ichnology

Pl - Planolites   Cy - Cylindrichnus
Pa - Palaeophycus   Rh - Rhizocorallium
Be - Bergaueria   Te - Teichichnus
Lk - Lockeia   Sk - Skolithos
Th - Thalassinoides   Fu - Fugichnia
Ph - Phycosiphon   Ch - Chondrites
Zo - Zoophycos

Fossils

Inoceramids   Fish Scales
Ammonites   Belemnites
Bivalves   Shark Teeth
Crustaceans

Other

ab. - abundant
org - organics   - Paleocurrent
shell frag - shell fragments   direction

Figure 22- Legend used for measured sections and facies analysis.
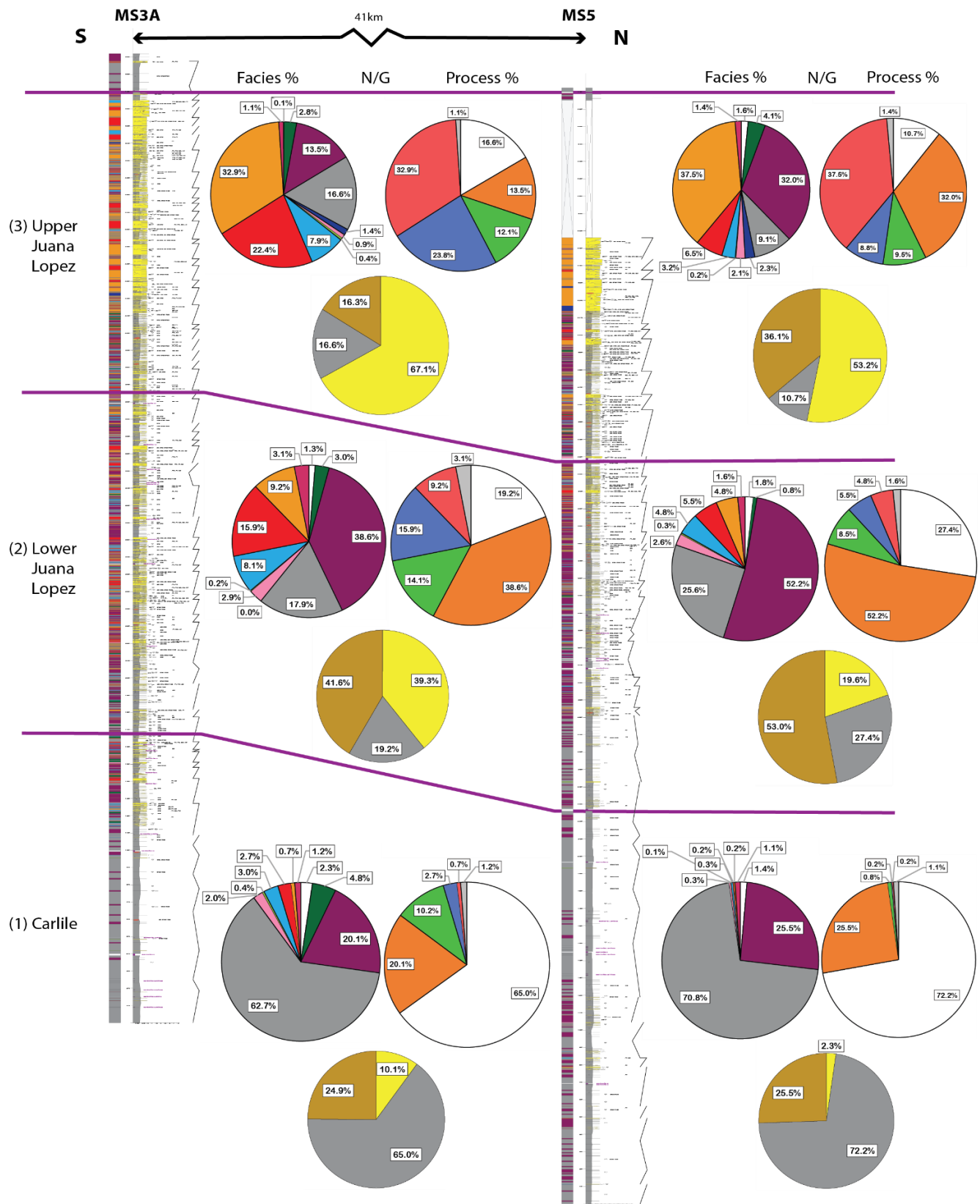
Figure 23– Vertical facies variability in 3 different portions (1) the Carlile Shale, (2) the lower Juana Lopez and (3) the upper Juana Lopez, between MS3A and MS5. In each section the upper pie charts are showing the proportions of facies (left pie chart) and the proportions of associated depositional processes (right pie chart), the lower pie chart is showing the sand-to-shale (N/G) ratios. Poster size shown in Appendix as Poster 1.

Table 1- Facies proportions (from Figure 23) observed in MS3A and MS5 in three vertically different stratigraphic portions along with their corresponding depositional processes. The various colours correspond to the depositional processes grouped in Table 2.

| | | Percentages (%) | | | | | |
| | | (1) Carlile | | (2) Lower Juana Lopez | | (3) Upper Juana Lopez | |
Facies	Process	MS3A	MS5	MS3A	MS35	MS3A	MS5
1) Bentonite	Suspension settling	2.3	1.4	1.3	1.8	0.1	1.6
2) Normally Graded	Ignitive turbidite	4.8	0.0	3.0	0.8	2.8	4.1
3) Planar Interlaminated Mudstone & Sandstone	Fluid muds/Tidal currents	20.1	25.5	38.6	52.2	13.5	32.0
4) Shaly Claystone	Suspension settling	62.7	70.8	17.9	25.6	16.6	9.1
5) Micro-hummocky Cross-stratified Sandstone	Tempestite	0.0	0.0	0.0	0.0	1.4	2.3
6) Planar Laminated Siltstone & Sandstone	Ignitive turbidite	2.0	0.3	2.9	2.6	0.9	2.1
7) Structureless Siltstone & Sandstone	Ignitive turbidite	0.4	0.1	0.2	0.3	0.4	0.2
8) Current Rippled Siltstone & Sandstone	Ignitive turbidite	3.0	0.3	8.1	4.8	7.9	3.2
9) Wave Rippled Siltstone & Sandstone	Tempestite	2.7	0.2	15.9	5.5	22.4	6.5
10) Combined Flow Rippled Siltstone & Sandstone	Wave modified turbidite/tempestite	0.7	0.2	9.2	4.8	32.9	37.5
11) Starved Rippled Siltstone & Sandstone	Unknown	1.2	1.1	3.1	1.6	1.1	1.4

Table 2 - Totaled depositional process proportions observed in in MS3A and MS5 in three vertically different stratigraphic portions.

| | Percentages (%) | | | | | |
| | (1) Carlile | | (2) Lower Juana Lopez | | (3) Upper Juana Lopez | |
Process	MS3A	MS5	MS3A	MS5	MS3A	MS5
Suspension Settling	65.0	72.2	19.2	27.4	16.6	10.7
Fluid muds/Tidal currents	20.1	25.5	38.6	52.2	13.5	32.0
Ignitive turbidite	10.2	0.8	14.1	8.5	12.1	9.5
Tempestite	2.7	0.2	15.9	5.5	23.8	8.8
Wave modified turbidite/tempestite	0.7	0.2	9.2	4.8	32.9	37.5
Unknown	1.2	1.1	3.1	1.6	1.1	1.4
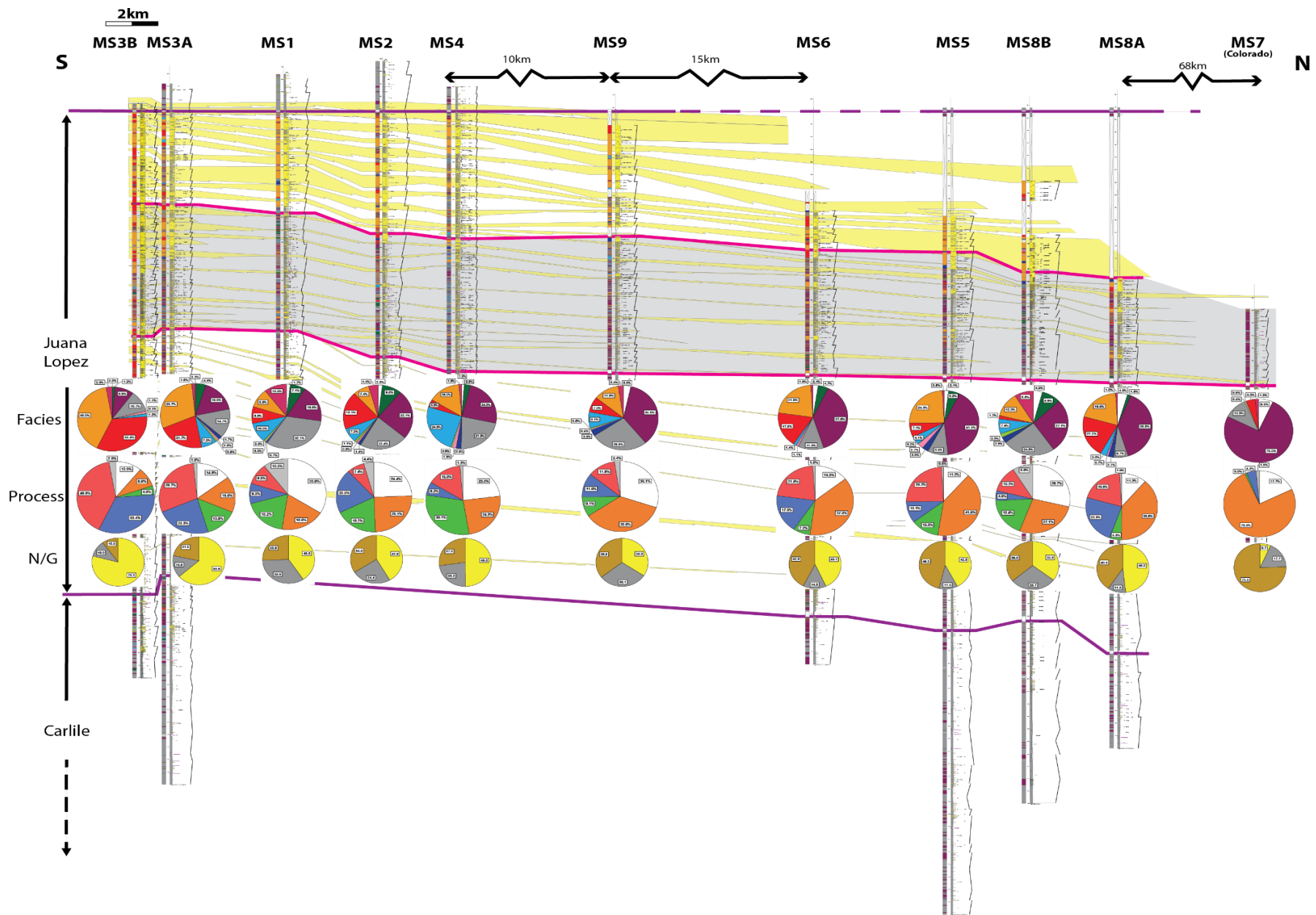
Figure 24- Juana Lopez measured sections from north to south with correlated stratigraphic area used for lateral facies analysis outlined with two pink lines and shaded in grey. Below the area are pie charts, the upper showing the proportions of facies in each section; the middle showing the proportions of associated depositional processes, and the lower showing the sand-to-shale (N/G) ratios. Poster size shown in Appendix as Poster 2.

Table 3- Facies proportions (from Figure 24) observed in the ten measured sections (going from south to north) along with their corresponding depositional process. The various colours correspond to the depositional processes grouped in Table 2.

Facies	Process	Percentages (%)										
		MS3B	MS3A	MS1	MS2	MS4	MS9	MS6	MS5	MS8B	MS8A	MS7
1) Bentonite	Suspension settling	0.2	0.1	1.7	2.0	1.2	3.5	2.4	2.1	4.2	4.6	6.8
2) Normally Graded	Ignitive turbidite	1.2	4.9	7.1	9.0	2.9	0.0	4.7	5.2	8.9	1.6	0.0
3) Planar Interlaminated Mudstone & Sandstone	Fluid muds/Tidal currents	8.8	16.6	18.6	25.1	24.3	35.6	37.8	41.0	27.1	38.9	75.5
4) Shaly Claystone	Suspension settling	10.7	14.7	32.1	22.4	21.8	26.6	11.9	9.5	24.5	6.7	10.9
5) Micro-hummocky Cross-stratified Sandstone	Tempestite	0.0	1.7	0.7	1.4	2.4	3.3	0.0	3.0	2.9	2.7	0.0
6) Planar Laminated Siltstone & Sandstone	Ignitive turbidite	1.1	1.0	0.3	0.9	1.8	0.4	1.1	2.7	0.0	0.7	0.4
7) Structureless Siltstone & Sandstone	Ignitive turbidite	0.3	0.8	0.8	1.1	0.6	0.5	0.0	0.2	2.0	0.0	0.5
8) Current Rippled Siltstone & Sandstone	Ignitive turbidite	1.5	7.2	10.0	7.3	24.8	8.1	1.4	4.1	7.4	3.0	0.0
9) Wave Rippled Siltstone & Sandstone	Tempestite	33.4	21.7	8.5	19.1	3.8	7.8	17.8	7.1	1.7	21.2	4.3
10) Combined Flow Rippled Siltstone & Sandstone	Wave modified turbidite/tempestite	40.0	29.7	9.6	7.4	15.0	11.8	21.8	24.3	12.3	19.6	0.0
11) Starved Rippled Siltstone & Sandstone	Unknown	2.8	1.6	10.5	4.4	1.3	2.4	1.0	0.8	8.8	1.0	1.5

Table 4- Totaled depositional process proportions observed in the eleven measured sections.

Process	Percentages (%)										
	MS3B	MS3A	MS1	MS2	MS4	MS9	MS6	MS5	MS8B	MS8A	MS7
Suspension Settling	10.9	14.8	33.9	24.4	23.0	30.1	14.3	11.5	28.7	11.3	17.7
Fluid muds/Tidal currents	8.8	16.6	18.6	25.1	24.3	35.6	37.8	41.0	27.1	38.9	75.5
Ignitive turbidite	4.0	13.9	18.2	18.2	30.1	9.1	7.2	12.2	18.4	5.3	0.8
Tempestite	33.4	23.3	9.3	20.5	6.2	11.0	17.8	10.1	4.6	23.9	4.3
Wave modified turbidite/tempestite	40.0	29.7	9.6	7.4	15.0	11.8	21.8	24.3	12.3	19.6	0.0
Unknown	2.8	1.6	10.5	4.4	1.3	2.4	1.0	0.8	8.8	1.0	1.5

6. Correlation

A photographic correlation (Fig. 25) was completed of a 350 m outcrop exposure photomosaic at MS8B, where bentonites, major flooding surfaces and sandstone dominated bedset surfaces were correlated. The correlated surfaces across the photomosaic can be traced across the northern Juana Lopez outcrop belt with high accuracy from MS8B to MS8A and from MS8B to MS5, covering a total distance of 6 km. This photographic bedding diagram demonstrates the ability to correlate key boundaries in the Juana Lopez with high confidence within a distance of at least 6 km. In the bedding diagram (Fig. 25) it is evident that bedset dominated sandstone surfaces (shown in black) increase in frequency when approaching a major flooding surface (shown in blue), indicative of a parasequence set.
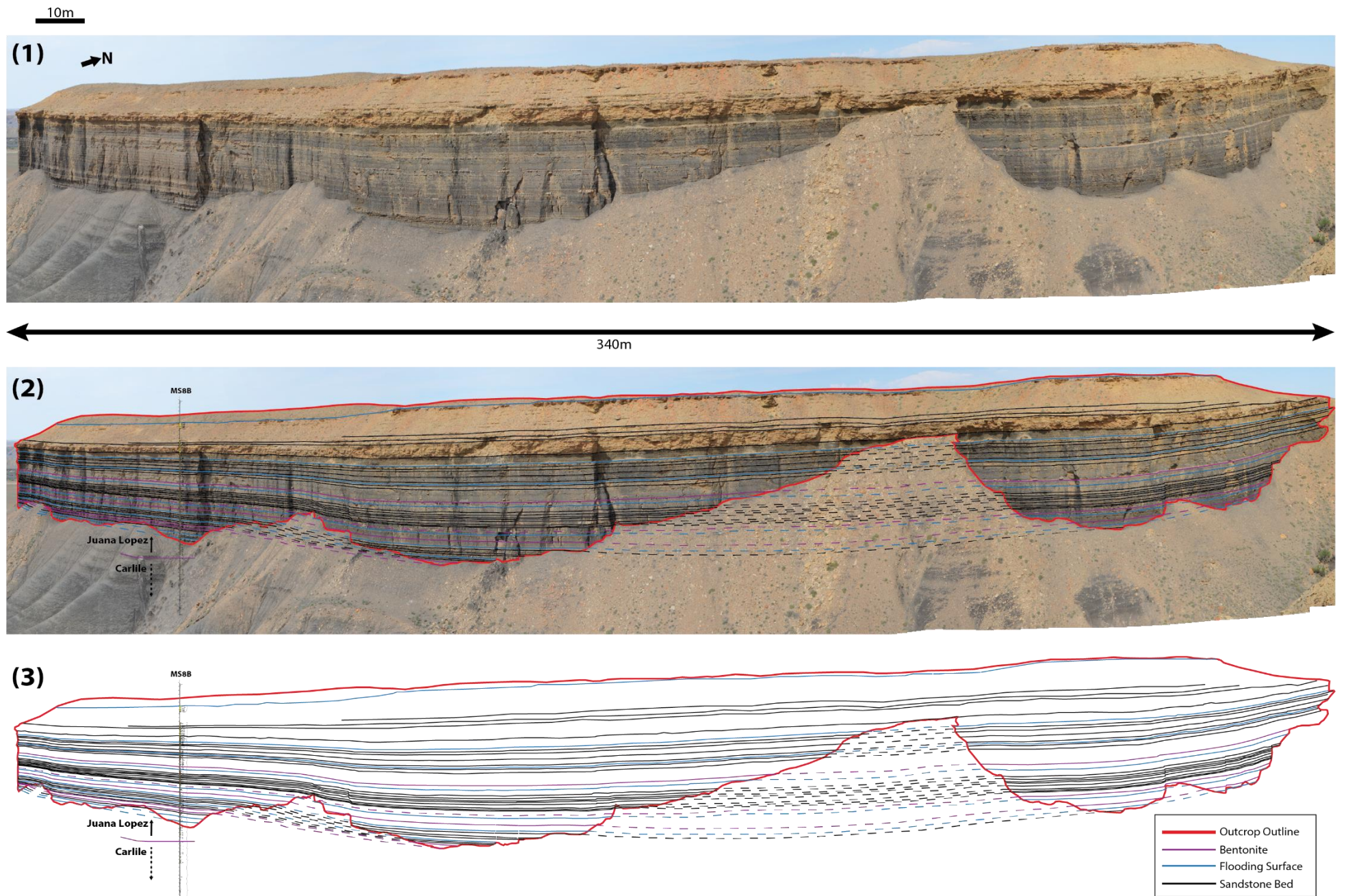
Figure 25– Juana Lopez bedding diagram at MS8B outcrop exposure. (1) Outcrop exposure, (2) outcrop exposure with bentonite, bedding and major flooding surfaces traced across, (3) bedding diagram.

Correlations of many mud-rich heterolithic marine units in the Cretaceous Western Interior Seaway, have been shown to contain recognizable clinoforms, progradation and lap-out deposition (Asquith, 1970; Leithold, 1994; Bhattacharya & Walker, 1991; Hampson, 2010; Birgenheier et al., 2017; Li & Schieber, 2018). The Juana Lopez correlation also shows evidence of more complicated progradational and retrogradational stacking patterns, as well as onlap and downlap geometries (Fig. 27).

4 sequences (S), 11 parasequence sets (PS), and 39 parasequences were identified in the Juana Lopez (Fig, 27). The number of parasequences vary between sections, however 39 parasequences refer to those found in MS3A, which contains the complete Juana Lopez stratigraphy. The 11 PS show the following stacking patterns: (i) aggradational (A), (ii) aggradational to progradational (AP), (iii) progradational to aggradational (PA), and (iv) retrogradational to aggradational (RA). The PS are bounded above by a major flooding surface or sequence boundary. Each set consists of a varying number of smaller-scale parasequences, which also vary laterally and show evidence of onlapping and downlapping geometries. These parasequences are more abundant in the south compared to the north. This is due to the thinning of top parasequence sandstone beds, which distally pinch-out or thin out to sandstone lamina (Fig. 27). With a collective time span of *ca* 1.2 myr, these Juana Lopez PS encompass an average of *ca* 110 kyr, likely representing Milankovitch-scale cycles of eccentricity.

PS 1

PS 1 has an average thickness of 6 m across the entire area and shows little thickness change towards the north. The number of coarsening-upward parasequences decreases southward from 8 to 1. This set undergoes a lateral facies change from more sandstone dominated bedsets in the south to more shelf mudstone heteroliths dominated in the north, with combined flow rippled

(F10) and wave rippled facies (F9) being dominant in the sandy bedsets. This set includes the most mud-rich sediments in the Juana Lopez. The overall stacking pattern shown in this set is aggradational to progradational (Fig. 27) suggesting overall regressive sedimentation. This set is capped by a sequence boundary above a wave rippled (F9) to combined flow rippled (F10) very fine lower sandstone bed with abundant amounts of inocermids, bivalves and ammonite fossils.

PS 2

PS 2 is a northward thinning wedge, passing from 8.5 to 4.5 m across the entire study area. The number of parasequences decreases towards the south from 9 to 3 as they pinch-out. This set has the most abundant and laterally extensive bentonite layers (F1), one of which correlates across the entire study area. Sediments tend to be richer in thinly bedded wave rippled very fine sandstones (F9) in the south, whereas planar interlaminated mudstone and sandstone (F3) dominated towards the north. This set shows an aggradational stacking pattern (Fig. 27) with no clear distinction of progradation or retrogradation, and downlaps the underlying sequence boundary. This set is capped by a major flooding surface distinguished by an obvious increase in clay content in the overlying shaly claystone facies (F4).

PS 3

PS 3 is 3 to 4 m thick, extends over the entire study area, and has no obvious thickening or thinning behaviour. This set contains 3 to 4 parasequences, which contain much thicker rippled sandstone dominated bedsets (F8, F9 and F10) in the south and very thin rippled sandstone dominated bedsets and lamina in the north. PS 3 contains a progradational to aggradational stacking pattern (Fig. 27) suggesting overall regressive sedimentation. PS 3 is capped by a major flooding surface on top of a rippled sandstone bed containing shell fragments and an overlying basinward facies shift.

PS 4

PS 4 is consistently thin and does not exceed 2.5 m. This set primarily consists of one parasequence; however in MS4, 3 parasequences were distinguished. An aggradational stacking pattern is shown with no clear distinction of progradation or retrogradation. This set is capped by a sequence boundary on top of a northward thinning rippled very fine lower sandstone bed. This sequence boundary is distinguished due to the onlapping of PS 5 onto this surface between MS1 and MS2.

PS 5

PS 5 is a northward thickening wedge between MS2 and MS7 with thickness increasing from 3 to 5.5 m. This set consists of mostly upward coarsening units with 3 to 4 parasequences. A major bentonite layer (F1) found in the upper part of PS 5 can be correlated across the entire set. Rippled very fine lower sandstone beds (F9 and F10) at the top of the parasequences thin out northward to very thin-bedded to lamina-scale sandstones. This set onlaps the underlying sequence boundary. PS 5 shows a progradational to aggradational stacking pattern (Fig. 27) and is capped by a major flooding surface with onlap above and is downlapped by PS6. PS 5 may be a distal expression of a major regression.

PS 6

PS 6 forms a wedge that pinches out northward between MS3B and MS9 with thickness decreasing from 3 to 0 m. Parasequences within this set vary from 2 to 5. Rippled sandstone beds (F8, F9 and F10) thin towards the north and downlap the underlying major flooding surface between MS9 and MS6. This set shows a retrogradational to aggradational stacking pattern (Fig. 27) and is capped by a major flooding surface. This retrogradational stacking pattern may represent the distal expression of transgression.

PS 7

PS 7 is 4 to 5 m thick and extends over the entire study area. The number of parasequences decreases from 6 to 2 northward as they pinch-out. Current rippled sandstone beds (F8) are abundant in the south and turn to combined flow rippled sandstone beds (F10) in the north suggesting wave reworking in the more distal area. PS 7 contains a progradational to aggradational stacking pattern (Fig. 27) suggesting overall regressive sedimentation. PS 7 is capped by major flooding surface on top of a combined flow rippled sandstone bed (F10). This combined flow rippled sandstone bed contains a lag deposit with an abundance of shell fragments, organic material and shark teeth found between MS9 and MS8A (Fig. 28).

PS 8

PS 8 has a constant thickness of approximately 2 m across the entire study are. This set consists of 1 to 3 parasequences. Combined flow rippled (F10) and wave rippled sandstone beds (F9) are a lot thicker in the south and thin or pinch-out northward. The proportion of current, wave and combined flow rippled sandstone facies (F8, F9 and F10) in PS 8 in the south is 90% compared to 50% in the north. An aggradational to progradational stacking pattern is shown in this set (Fig. 27). This set is capped by a sequence boundary on top of a wave rippled dominated very fine lower sandstone bed (F9). This sequence boundary is interpreted on the basis of onlapping of PS 9 onto this surface between MS1 and MS2.

PS 9

PS 9 seems to have a lobate structure. This set is a northward and southward thinning wedge between MS2 and MS8A with thickness decreasing from 2.5 m to 0.5 m to the south and from 2.5 m to 0.2 m to the north. This set consists of 2 parasequences that thin out to 1 parasequence in both directions. This set onlaps the underlying sequence boundary between MS1 and MS2 and

most likely downlaps onto the sequence boundary further north of MS8A. PS 9 consists of an aggradational to progradational stacking pattern (Fig. 27) and is capped by an onlapping major flooding surface. Similarly to PS 5, PS 9 may be a distal expression of a regression.

PS 10

PS 10 is 3.5 to 5 m thick. Parasequences decrease from 8 at MS3A to 2 at MS8B as they pinch-out. PS 10 consists of thick rippled to micro-hummocky cross-stratified sandstone beds (F5) which seem to amalgamate towards the north. This amalgamation could be the result of erosion, pinch-out of shelf mudstone heteroliths or non-deposition. PS 10 contains a progradational to aggradational stacking pattern (Fig. 27) suggesting overall regressive sedimentation. PS 10 is capped by a major flooding surface on top of a micro-hummocky cross-stratified sandstone bedset (F5) containing an abundance of shell fragments, inoceramids and organics (Fig. 29)

PS 11

PS 11 is the final PS found in the Juana Lopez. PS 11 seems to thicken northward from 5 to 7 m. This set has the highest proportion of very fine lower to upper sandstone dominated bedsets, which are mostly combined flow rippled (F10). Sandstone bedsets are not correlated throughout the entire area due to missing data in the north, caused by erosion. However, in contrast to PS 10, sandstone units seem to amalgamate southward, and downlap to the north. The stacking pattern for PS 11 is aggradational to progradational (Fig. 27) suggesting a regressive unit. This set is capped by the final major flooding surface in the Juana Lopez, above which a major basinward shift of facies is found.

The majority of PS in the Juana Lopez show AP and PA stacking patterns (Fig. 27). Strictly A stacking patterns are also identified in two of the eleven PS, where no distinct progradation or retrogradation could be differentiated. RA accounts for a minor volume of the

deposits and is only found in PS 6, and may represent a transgressive systems tract. Overall, the

Juana Lopez is dominated by upward-shoaling PS with an increasing number and thickness of

sandstone dominated bedsets, suggesting overall regressive sedimentation. Transgressions are

interpreted in PS 6 and PS 10 and may represent lowstand systems tracts.

Correlations

- - - - - - - - - - - Calcareous Nodules

————————— Bedset Boundaries

————————— Bentonite

————————— Flooding Surfaces

————————— PS Bounding
Major Flooding Surfaces

————————— PS Bounding
Sequence Boundary

☐ Sandstone Dominated Bedsets

☐ Shelf Mudstone Heteroliths
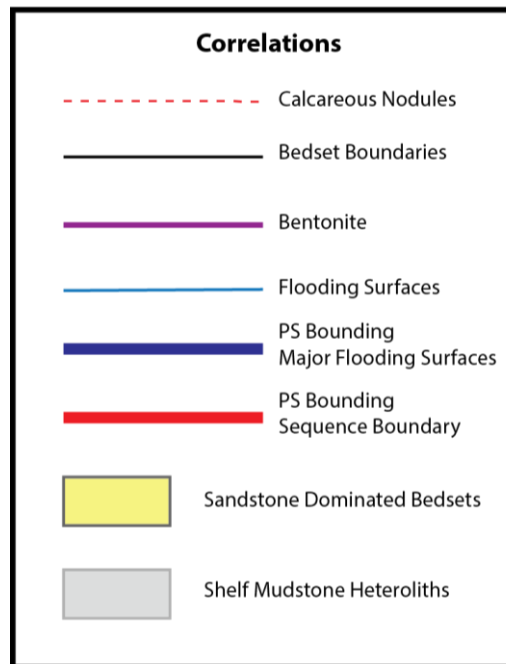
Figure 26 - Legend associated with correlation surfaces and units in Figure 27.
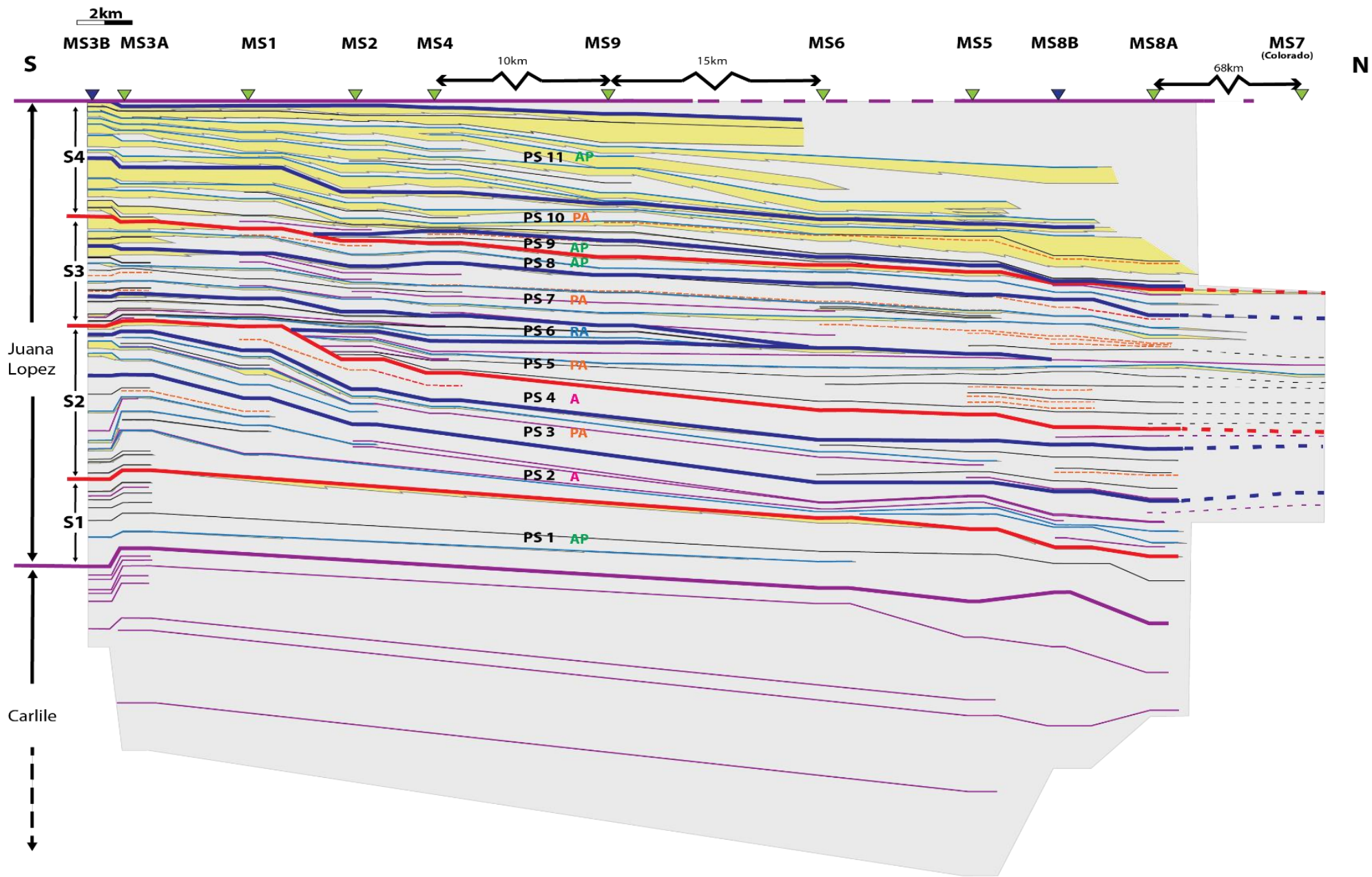
Figure 27 - Juana Lopez correlations, associated sequences, parasequence sets and stacking patterns, as well as bentonite correlations in the Carlile Member of the Mancos Shale. Legend shown in Figure 26. Poster size shown in Appendix as Poster 3.
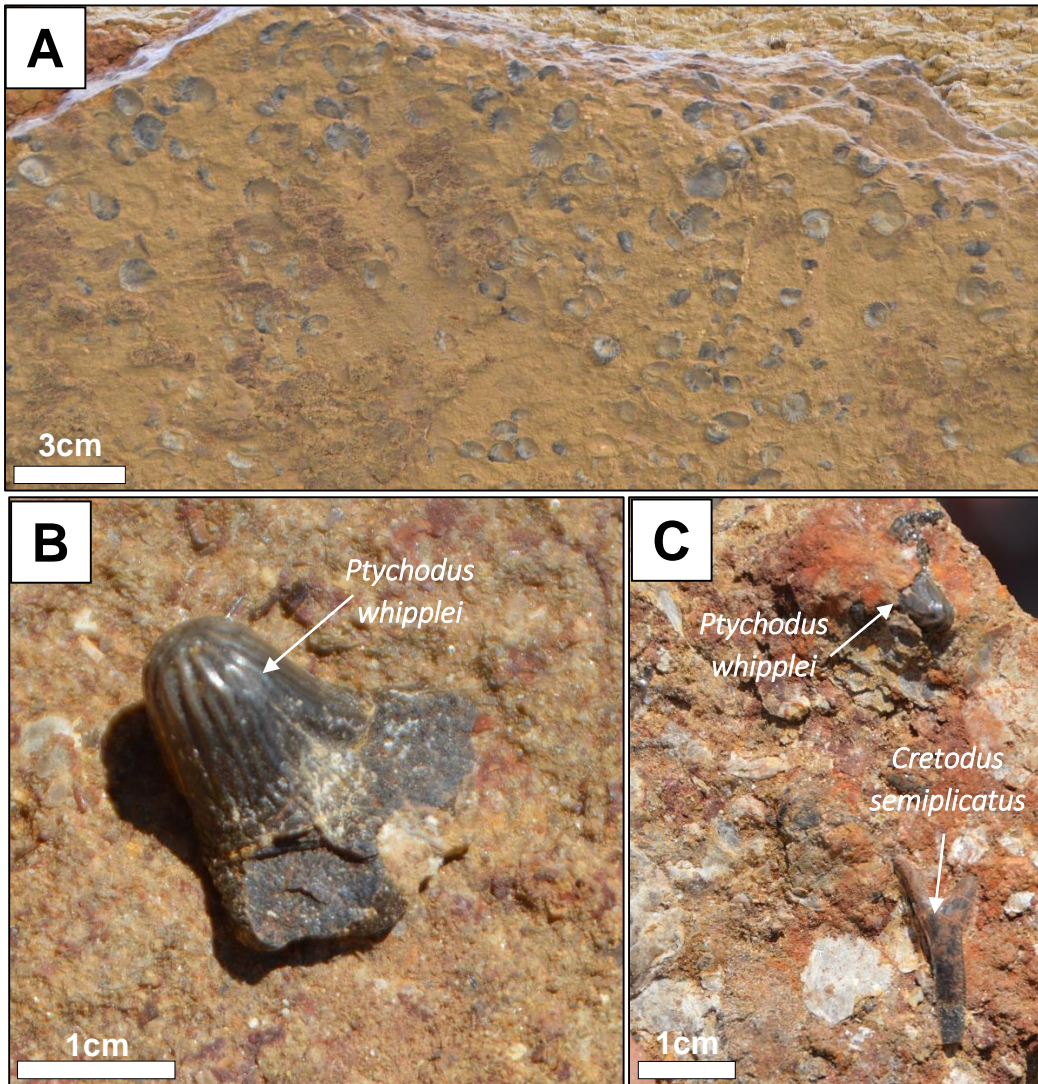
Figure 28 - Very fine upper sandstone lag deposit found at the top of PS 7 with an abundance of A) bivalves and shark teeth B) *Ptychodus whipplei* and C) *Cretodus semiplicatus* (shark tooth fossil identification taken from Sealey & Lucas, 2006).
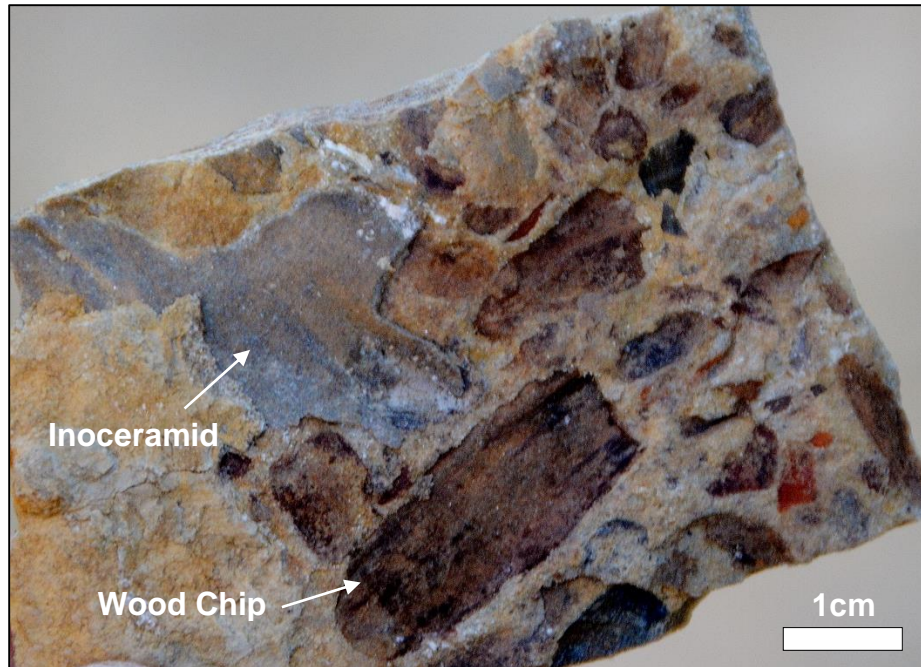
Figure 29 - Abundance of inocermaid fragments, shell fragments, organic material and wood chips in a very fine lower sandstone lag deposit capping PS 10.

7. Paleocurrent Data

Paleocurrent measurements of unidirectional and oscillatory flows from all eleven measured sections are shown on Rose Diagrams in Figure 30. A total of 520 paleocurrent measurements were made, with the highest number (79) recorded in MS1. An average of 23 unidirectional paleocurrent directions and 29 wave crest directions were measured in each section.

Palaeoenvironmental reconstruction of the Western Interior Seaway during the Late Cretaceous suggests circulation was controlled mainly by storms, waves and tidal currents (Ericksen & Slingerland, 1990; Slingerland & Keen, 1999). The mean annual wind field, latitudinal temperature gradient, and freshwater runoff also created a background circulation of geostrophic flows (Slingerland & Keen; 1999). On the western shoreline, these controls produced dominantly southward-directed alongshore currents and net sediment drift to the south (Fig. 31) (Barron, 1989; Ericksen & Slingerland, 1990; Slingerland & Keen, 1999). In addition, a

Coriolis driven counter-clockwise circulation gyre in the seaway deflected sediment southward along the western shelf and may have formed mud belts that may extend 1000s of kilometers along-shelf (Fig. 31) (Duke, 1990; Kineke et al., 1996; Nittrouer et al., 1996; Correggiari et al., 2005; Fielding, 2010; Plint et al., 2012)

Unidirectional paleocurrent directions recorded in this study, from current rippled laminations, show a dominant SE flow direction (Fig. 30). This SE flow may represent southward-directed along-shelf currents hypothesized to dominate the seaway during the Cretaceous. Less prevalent eastern flows are also recorded, mostly from the top sandstone dominanted bedsets in PS 10 and PS 11. Oscillatory paleocurrent directions recorded from wave rippled laminations show a NE-SW flow direction, which runs perpendicular to the Turonian shoreline (Fig. 30). Similar paleocurrents are shown in the overlying Gallup Formation (Krueger, 2010). Krueger (2010) recorded 890 paleocurrent measurements in the Gallup, which determined a NE-SW dominated oscillatory flow and SE dominated longshore currents, with NW dominated currents in the river deposits.
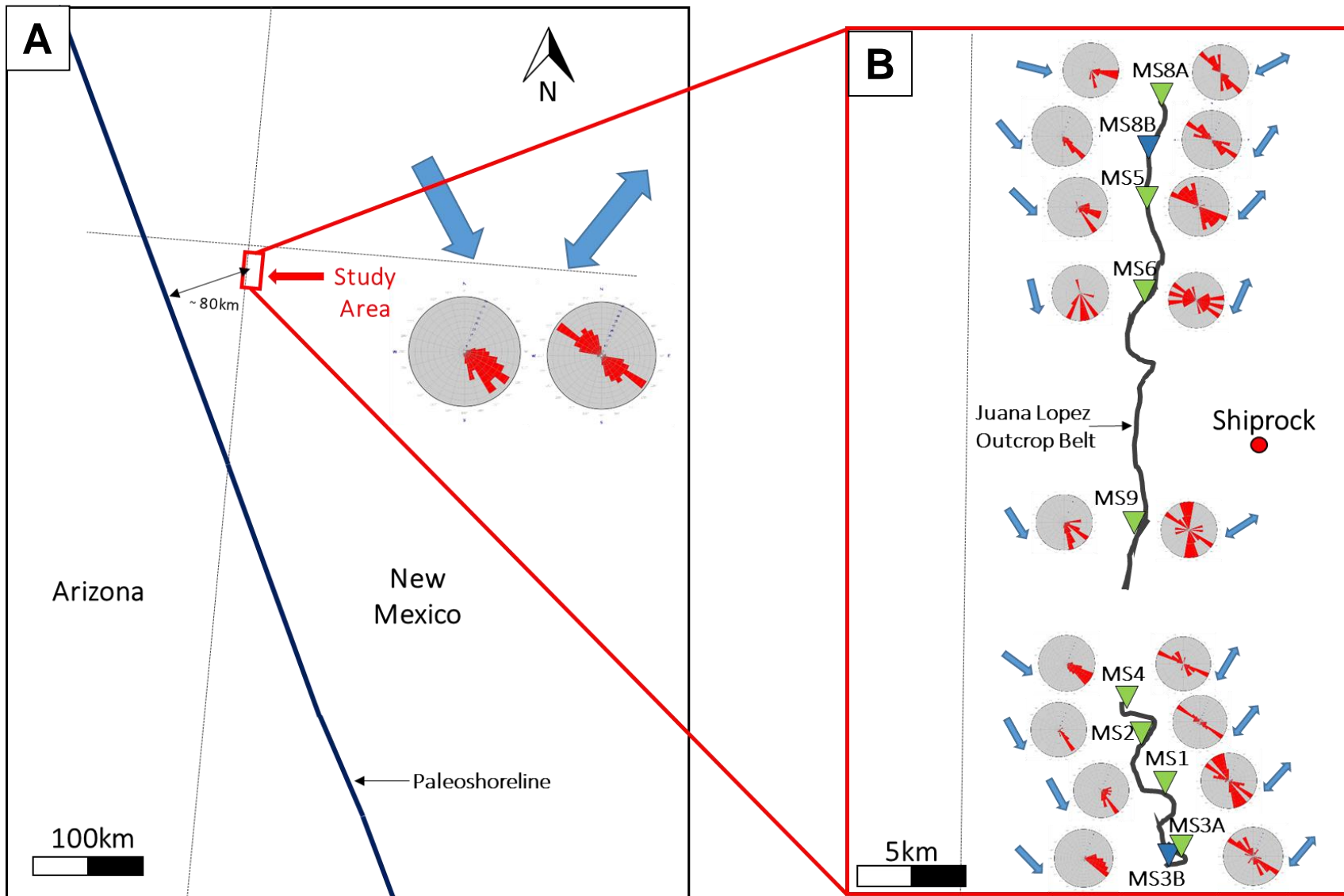
Figure 30 - A) Study area shown in relation to early Late Turonian transgressive shoreline, taken from Molenaar (1983). Paleocurrent measurements shown in Rose Diagrams for all sections combined. Blue arrows show dominant SE unidirectional flow direction and dominant NE-SW oscillatory flow direction in the Juana Lopez. B) Paleocurrent measurements shown in Rose Diagrams for each measured section along the Juana Lopez outcrop belt. Rose Diagrams on the left represent paleocurrent directions recorded from current rippled laminations, and wave crest directions on the right. Neighbouring blue arrows show dominant paleocurrent directions in each Rose Diagram.
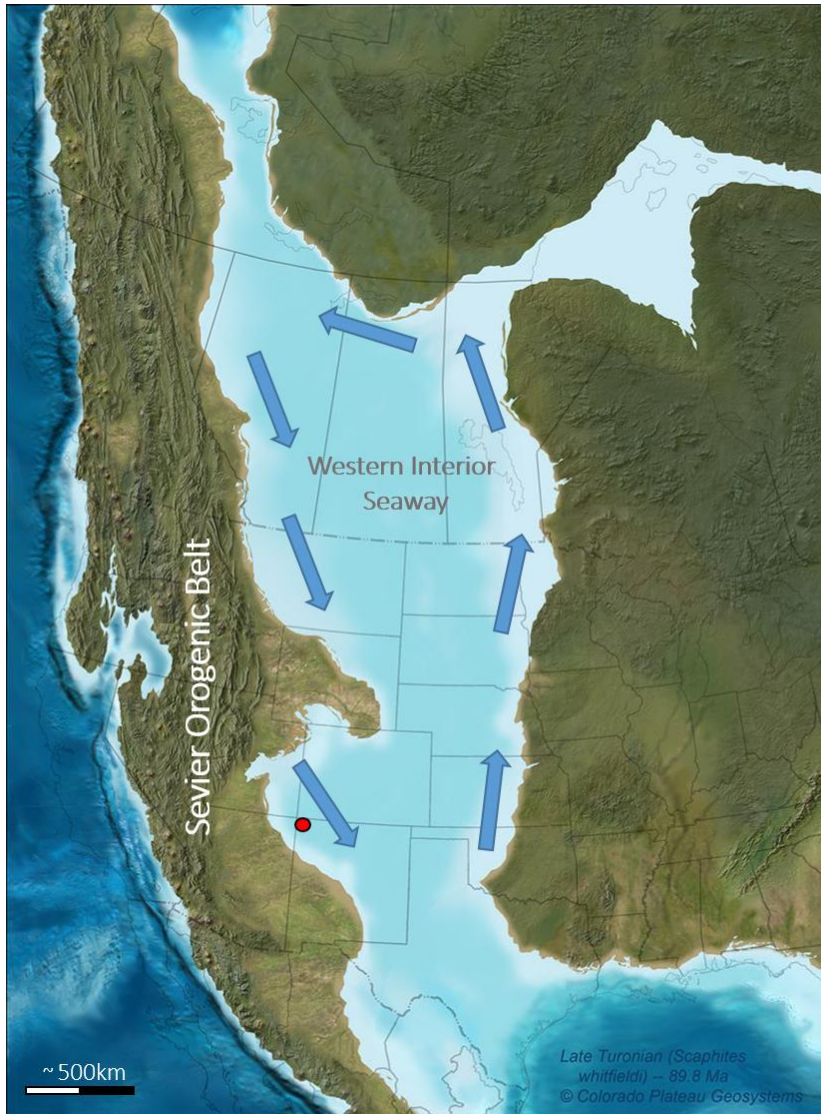
Figure 31– Late Turonian paleogeographic map of the Western Interior Seaway (Blakey, 2014). Blue arrows show generalized circulation of flow within the seaway (taken from Ericksen & Slingerland, 1990; Slingerland & Keen, 1999). Dominant southward-directed alongshore currents are seen along the western margin of the seaway. Study area shown by red dot.

8. Discussion

8.1 Sediment Source

Dominant unidirectional paleocurrent measurements suggest the source of silt and sand feeding the Juana Lopez to be moving from the NW and along-shelf in a SE direction. Therefore, sediment entering the seaway from proximal Turonian clastic wedges found northwest of the study area are most likely traveling as an intershelf mudbelt and depositing into the San Juan

Basin. As shown in Fig. 1, the Cretaceous Western Interior Seaway has several Middle to Late Turonian, fluvio-deltaic clastic wedges found northwest of the study area. Assuming fine-grained sediment traveled along-shelf within 1000 km along the shoreline, the possible clastic wedges feeding the Juana Lopez include the Ferron Sandstone Member of the Mancos Shale, which is informally divided into the Notom, Last Chance and Vernal Deltas in Utah, and the Tibbet Canyon Member of the Straight Cliffs Formation of the Kaiparowits Delta in Southern Utah.

The Ferron Sandstone is an eastward prograding fluvial-deltaic system that consists of both nonmarine river-dominated delta-plain deposits and genetically related shallow-marine deposits (Peterson and Ryder, 1975; Garrison & van den Bergh, 2004; Li et al., 2015; Fielding, 2010; Zhu et al., 2012). In the Uinta Basin of Utah, the Ferron Sandstone is proximally equivalent to the Juana Lopez (Fig. 32. River-fed hyperpycnal flows originating from the eastward directed Ferron Sandstone encountered the counter-clockwise Coriolis forces, which would have deflected sediment to the south, eventually depositing into the San Juan Basin (Molenaar & Cobban, 1991; Anderson & Harris, 2006; Birgenheier et al., 2017; DeReuil & Birgenheier, 2018).

The Tibbet Canyon Member of the Straight Cliffs Formation consists of regressive northeast prograding shoreface sandstones and tidally influenced channel deposits (Eaton, 1991; Shanley & McCabe, 1991). In the Kaiparowits Basin, the Tibbet Canyon Member is proximally equivalent to the Ferron Sandstone and Juana Lopez Member (Fig. 33) (Molenaar; 1983; Eaton, 1991; Shanley & McCabe, 1991).

Sandstone dominated bedsets in the upper Juana Lopez show a more easterly unidirectional paleocurrent flow direction, which are most likely fed by the east Lower Gallup Atarque Member (Fig. 4). The Lower Gallup Atarque Member is found in the Zuni Basin and

consists of a regressive coastal barrier sequence, which correlates with the upper portion of the

Juana Lopez in the San Juan Basin (Molenaar, 1973). The oldest Upper Gallup F tongue (shown

in Fig. 4) in the San Juan Basin lies in the late Turonian *Scaphites whitfieldi* ammonite zone, in

which the upper portion of the Juana Lopez also lies. Therefore, it is suggested that the

northeastern progradation of the updip Gallup Sandstone commenced and could have fed the

basinward accumulating Juana Lopez, also possibly explaining the more east-directed

paleocurrents in the top sandstone dominated bedsets. In addition, the increase in unidirectional

flows and turbidite deposits between MS1 and MS4 (shown in the lateral facies analysis Fig. 24)

may suggest the proximity to the easterly prograding Atarque Member and Gallup F tongue delta

source.
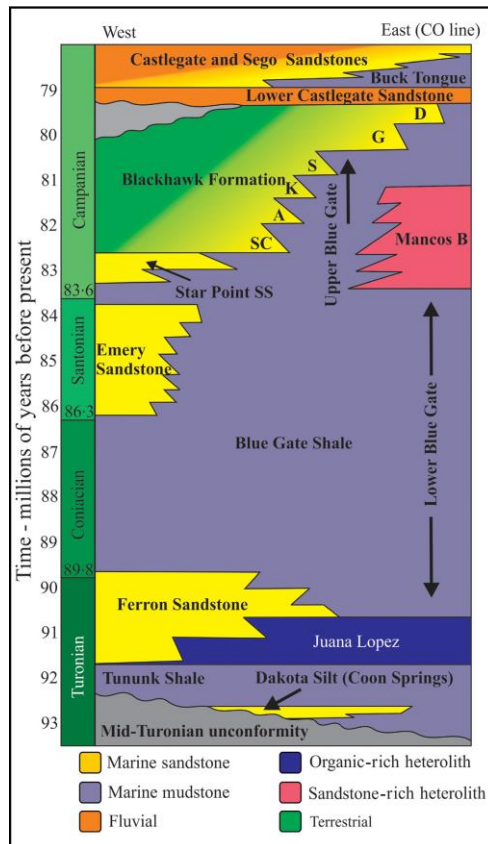
Figure 32– West to east relative positions and chronology of the Mancos Shale members in the Uinta Basin (taken from Birgenheier et al., 2017). The Ferron Sandstone is shown as being proximally equivalent to the Juana Lopez Member.
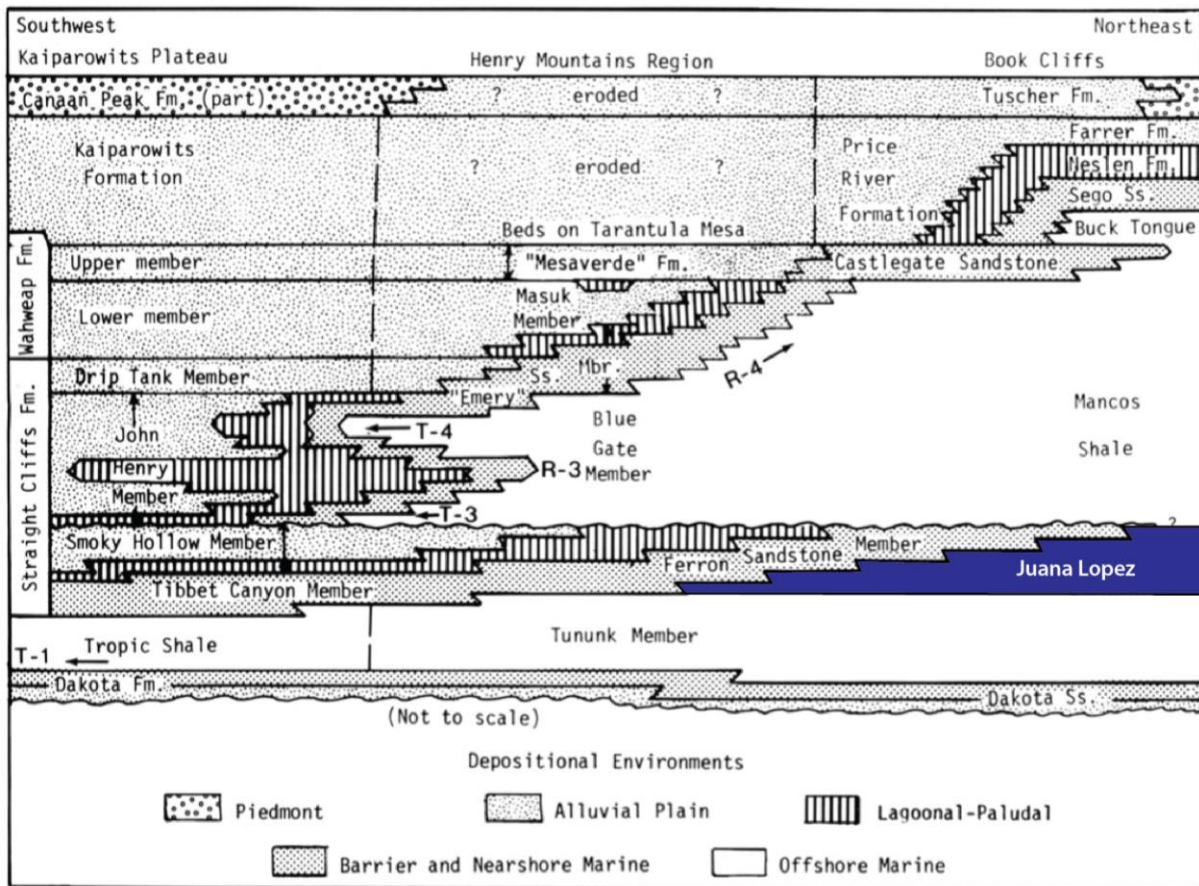
Figure 33 - Schematic stratigraphic cross-section through the Kaiparowits Plateau, the Henry Mountains Region and the Book Cliffs (Taken from Molenaar, 1983, modified from Peterson et al., 1980).

8.2 Depositional Model

High-resolution facies analysis, with corresponding paleogeography and paleocurrent data indicates that the fine-grained sediment of the Juana Lopez was deposited by both along- and across-shelf currents onto a storm-dominated mudbelt, where resuspension by wind, storms and tides took place before final deposition (Fig. 34).

The mudbelt depositional environment is composed of fine-grained sediment that is initially supplied by rivers and advected along-shelf by geostrophic and longshore currents (Plint, 2014; Birgenheier et al., 2017; DeReuil & Birgenheier, 2018). The sediment was then resuspended by storm waves on the shelf, which generated sediment gravity flows that

transported the sediment further across the shelf (Macquaker et al., 2010; Schieber, 2016; Birgenheier, 2017). Recent studies on ancient mudbelt deposits (e.g. Birgenheier et al. (2017), and Li and Schieber (2018)), and modern mudbelt deposits (e.g. Liu et al. (2006) and Liu et al. (2018)) determine sediments to be transported up to 800 km along-shelf, and 100 km offshore, with dominant grain size of silt to clay (less than 62.5 µm) and an upper grain size limit of very fine sand (less than 125 µm).

Above storm wave base, on the proximal part of the mudbelt, sandstone-dominated bedsets of the upper Juana Lopez, which contain combined, current or wave rippled laminations, or in some cases micro-hummocky cross-stratification, are deposited by storm surges, wave-enhanced sediment gravity flows and geostrophic flows (as shown in Facies 5, 8, 9 and 10). The dominance of sandstone (grain size less than 125 µm) suggests deposits to be closer to a river source (Liu et al., (2006); Liu et al., (2018))

Distal mudbelt deposits consist of shaly claystones, interlaminated mudstones and sandstones with discontinuous laminations, scours and starved-rippled siltstone and very fine lower sandstone laminations (as shown in Facies 3, 4 and 11). These deposits formed through resuspension due to storms, wave and current enhanced sediment gravity flows, as well as tidal and along-shelf currents. These heterolithic deposits contain basal scour surfaces, and traction features, such as ripples and normal grading (as shown in Facies 3 and 6).

Mudbelts are known to extend hundreds of kilometers alongshore and tens of kilometers, and in some cases over 100 km, across the basin (Nittrouer et al., 1986; Kuehl et al., 1997; Allison et al., 2000; Liu et al., 2007; Birgenheier et al., 2017). According to the maximum transgressive paleoshoreline of the Late Turonian (Fig. 31, taken from Molenaar, 1987), the study area of the Juana Lopez lies about 80 km into the basin. Therefore, in this study the

mudbelt environment is considered to be at least 80 km wide. This mudbelt width is consistent with a basinward reach of current and wave enhanced sediment gravity flows, proposed by Schieber (2016), being on the scale of 100 km.

In general, grain size and BI decreases from the proximal to distal mudbelt facies. The low BI indicates high sedimentation in a possibly stressed environment, which has been hypothesized to infer anoxic conditions (e.g. Rhoads & Morse, 1971; Wignall, 1991; Martin, 2004; Laurin & Sageman, 2007). However, the abundance of rapid deposition of interlaminated mudstones and sandstones, fluid muds, graded beds, rippled siltstones and sandstone, as well as calcareous (inoceramids, ammonites and bivalves) and biogenic material (fish scales), and the presence of bioturbation suggests that simple suspension settling in a reduced oxygenated basin was not an important component of deposition in the mudbelt of the Juana Lopez. Instead, the mudbelt displays evidence of dynamically deposited sedimentary structures along with preserved trace fossils, and calcareous and biogenic material in an oxic-suboxic environment (DeReuil & Birgenheier, 2018).
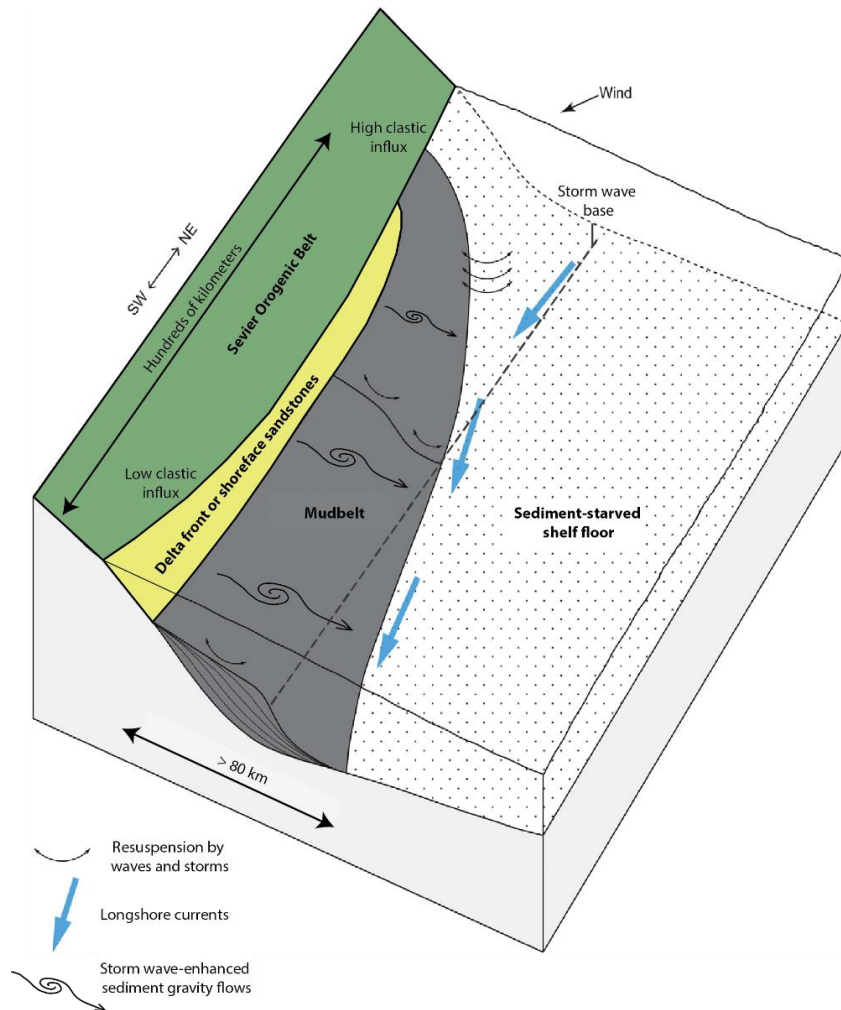
Figure 34 - Schematic illustration of the depositional model for the Juana Lopez Member. Majority of sediment supply is from updrift Middle to Late Turonian wedges (Ferron Sandstone and Tibbet Canyon Member of the Straight Cliffs Formation). This diagram is based on the results of this study and from models proposed for analogous mud-rich shelves supplied by longshore-currents (Allison et al., 2000; Schieber, 2016; Birgenheier et al., 2017; Li & Schieber, 2018) (modified from Li & Schieber, 2018).

8.3 Nature of Cyclicity

4 sequences, 11 parasequence sets, and 39 parasequences were identified in the Juana

Lopez. Given an overall time of *ca* 1.2 myr, the sequences, parasequence sets and parasequences

encompass an average of *ca* 300 kyr, *ca* 110 kyr and *ca* 30 kyr, respectively.

High-frequency stratigraphic cycles, have been recognized in several clastic wedges in

the Cretaceous Western Interior Seaway, such as the Ferron Sandstone in southern Utah

(Garrison & van den Bergh, 2004; Zhu et al., 2012) and the Tres Harmanos Formation in southern New Mexico (Mack et al., 2015). These studies provide clear evidence of glacio-eustatic Milankovitch cycles in the Turonian Western Interior Seaway. These studies reveal the frequency of the Milankovitch cycles to be approximately 50 to 300 kyr; therefore, the Juana Lopez cyclicity likely represents Milankovitch cycles.

In reference to broader Cretaceous cyclostratigraphy, many studies have confirmed that the observed Milankovitch-scaled cyclicity in the Cretaceous must be controlled by glacio-eustasy (Schwarzacher & Fischer, 1982; Barron et al., 1985; Fischer et al., 1985; Plint 1991; Gale et al., 2002; Miller et al., 2003, 2004, 2005).

With complete analysis from the Upper Cretaceous Russian platform and the New Jersey margin, Miller et al. (2003, 2004, 2005) concludes that the only known mechanism for the observed rapid, sub-million-year, sea-level changes in excess of 10 m or less is glacioeustasy since other hypothesized mechanisms are too small or too slow. Even though geological evidence points to warm high-latitude temperatures during the Upper Cretaceous, Miller et al. (2005) proposes Late Cretaceous to early Eocene ephemeral glaciers to be restricted in area in Antarctica, and paced by Milankovitch forcing.

Early studies have also supported a glacio-eustatic control in the Cretaceous, studies such as Schwarzacher and Fischer (1982), Barron et al. (1985), and Plint (1991). Schwarzacher and Fischer (1982) analyzed depositional rates of Carboniferous and Cretaceous limestones bundles in Ireland and Italy and confirmed a correlation of cyclicity with the Earth's 100 kyr short cycle in eccentricity, with the control being sensitive fluctuations in ice volumes. Similarly, Barron et al. (1985) confirmed average cyclicity of about 40 kyr in the Cenomanian-Turonian Greenhorn Cyclothem in the Western Interior Seaway, which corresponds remarkably well with climate and

63

orbital model simulations. This frequency again supports climate-driven Milankovitch scaled

cyclicity. Finally, Plint (1991) identified 15 regionally correlated parasequences in the

Coniacian-Santonian Muskiki and Marshybank Formations in Alberta to have an average

frequency of about 100 kyr. Plint (1991) argues that this frequency of cyclity is controlled by an

orbital forced glacio-eustatic mechanism rather than changes in subsidence or sediment-supply

rates.

With similar Milankovitch cyclicity found in the Upper Cretaceous Juana Lopez, the *ca*

30 kyr to *ca* 300 kyr cycles are interpreted to be glacio-eustatic in origin, which supports the

presence of ephemeral glaciers in the Cretaceous Period.

8.4 Hydrocarbon Reservoir Potential

There is an increasing demand to understand, explore, and exploit thin-bedded

heterolithic reservoirs, in which hydrocarbons found in sandstone beds are below the resolution

of conventional logging tools, or are found in mud-rich deposits (Schieber et al., 2007; Wilson &

Schieber, 2014). The detailed facies analysis and regional correlation of the Juana Lopez

provides an analog to oil and gas industries that documents the vertical and lateral variability of

heterolithic successions, which can increase production and profitability of unconventional

hydrocarbon resources. In addition, observing the vertical and lateral changes in facies and

depositional processes provides insight into minor and major geochemical changes, as well as

permeability and porosity changes in potential reservoir seal pairs.

The mudbelt deposits of the Juana Lopez are prospective heterolithic hydrocarbon

resources due to the elevated organic and carbonate content. Observing the lateral heterogeneity

of potential hydrocarbon filled sandstone reservoirs in the Juana Lopez is important in further

determining their extent of profitability. The upper PS of the Juana Lopez (PS 10 and PS 11) are

64

abundant in very fine lower to very fine upper sandstone dominated bedsets that commonly

pinch-out to the north (Fig. 27). The thickness of the sandstone packages in PS 10 and PS 11

ranges from 0.05 m to 2.5 m, and have a width of 2 km to 47 km (extend throughout the entire

New Mexico study area) (Fig. 27). The largest amalgamated sandstone package, with a thickness

of 2.5 m, is found between MS5 and MS8A in PS 10 (Fig. 27). These laterally extensive

sandstone packages can be potential hydrocarbon reservoir targets that are worth exploring.

9. Conclusion

The Juana Lopez Member in the San Juan Basin exhibits a variety of facies produced by

a number of depositional processes, allowing fine-grained sediments, carbonate material and

organics to be moved at least 80 km offshore. A total of 11 facies, 4 sequences, 11 parasequence

sets, and 39 parasequences are observed. Vertical and lateral facies analysis indicates an overall

regressive environment; however, observations of stacking patterns and lap-out relationships in

the regional correlation show evidence of transgressive cycles in PS 6 and PS 10. 520

paleocurrent measurements, along with the lateral facies analysis suggest the source of sediment

to be from easterly prograding Ferron Sandstone and Tibbet Canyon Member of the Straight

Cliffs Formation found NW of the San Juan Basin, as well as the Lower Gallup Atarque Member

and F Tongue of the Gallup, east of the San Juan Basin. The Juana Lopez is interpreted to be

deposited above storm wave base on a high energy oxic-suboxic mudbelt. The lower

heterolithics-dominated Juana Lopez is deposited on the distal mudbelt, where the dominant

depositional processes include suspension settling from geostrophic and along-shelf currents, as

well as tides; whereas, the upper sandstone-dominated Juana Lopez on the proximal mudbelt,

closer to a river source, where the dominant depositional processes include turbidity currents,

storm surges, wave-enhanced sediment gravity flows and geostrophic flows. Most of the upper

sandstone dominated bedsets are correlated to be at least 47 km wide with thicknesses ranging from 0.05 m to 2.5 m, and may be potential hydrocarbon reservoir targets that are worth exploring.

References

Aigner, T. (1982). Calcareous tempestites; storm-dominated stratification in upper Muschelkalk

limestones (Middle Trias, SW-Germany). *Cyclic and event stratification*, 180-198.

Aigner, T., & Reineck, H.E. (1982). Proximality trends in modern storm sands from the

Helgoland Bight (North Sea) and their implication for basin analysis. Senkenb. *Maritima*

14, 183-215.

Allen, J.R.L. (1969). On the geometry of current rippled in relation to stability of fluid flow.

Geografiska Annaler. Series A, Physical Geography, 51(1/2), 61-96.

Allison, M.A., Lee, M.T., Ogston, A.S., & Aller, R.C. (2000). Origin of Amazon mudbanks

along the northeastern coast of South America. *Marine Geology 163*, 241–256.

Anderson, D.S. (2010). Depositional Controls on the Organic-Rich Juana Lopez Member of the

Mancos Shale, Southeastern Basin, Utah. *AAPG Search and Discovery*.

Anderson, D. S., & Harris, N.B. (2006). Integrated sequence stratigraphic and geochemical

resource characterization of the Lower Mancos Shale, Uinta Basin, Utah. *Utah*

Geological Survey Open File Repor,t 483, 129.

Arnott, R.W.C. (1993). Quasi-planar-laminated sandstone beds of the lower Cretaceous

Bootlegger Member, north-central Montana: evidence of combined-flow sedimentation.

Journal of Sedimentary Petrology, 63(3), 488-494.

Asquith, D. O. (1970). Depositional topography and major marine environments, Late

Cretaceous, Wyoming. *AAPG Bulletin, 54*(7), 1184-1224.

Barron, E.J. (1983). A warm, equable Cretaceous: the nature of the problem. *Earth-Science*

Reviews, 19, 305–338.

Barron, E.J. (1989). Severe storms during earth history. *Geological Society of America Bulletin,*

101, 601–612.

Barron, E.J., Arthur, M.A., & Kauffman, E.G. (1985). Cretaceous rhythmic bedding sequences: a

   plausible link between orbital variations and climate. *Earth and Planetary Science*

   Letters, 72, 327-340.

Bates, C. C. (1953). Rational Theory of Delta Formation. *Bulletin of the American Association of*

   Petroleum Geologists, 37(9), 2119–2162.

Bentley, S.J. (2003). Wave-current dispersal of fine-grained fluvial sediments across continental

   shelves: the significance of hyperpycnal plumes. In: Scott, E.D., Bouma, A.H., Bryant,

   W.R. (Eds.), Siltstones, Mudstones and Shales: Depositional Processes and

   Characteristics. *SEPM/GCAGS Joint Publication*, 35-48.

Bhattacharya, J.P. (2011). Practical problems in the application of the sequence stratigraphic

   method and key surfaces: integrating observations from ancient fluvial–deltaic wedges

   with Quaternary and modelling studies. *Sedimentology, 58*, 120–169.

Bhattacharya, J. P., & Walker, R. G. (1991). Allostratigraphic subdivision of the Upper

   Cretaceous Dunvegan, Shaftesbury, and Kaskapau formations in the northwestern

   Alberta subsurface. *Bulletin of Canadian Petroleum Geology, 39*(2), 145-164.

Bhattacharya, J. P., & MacEachern, J. A. (2009). Hyperpycnal rivers and prodeltaic shelves in

   the cretaceous seaway of north america. *Journal of Sedimentary Research, 79*(4), 184-

   209.

Birgenheier, L.P, Horton, B., McCauley, A.D., Johnson, C.L., & Kennnedy A. (2017). A

   depositional model for offshore deposits of the lower Blue Gate Member, Mancos Shale,

   Uinta Basin, Utah, USA. *Sedimentology, 64*, 1402-1438.

Blakey, R.C. (2014). Paleogeography and Paleotectonics of the Western Interior Seaway,

Jurassic-Cretaceous of North America. *AAPG Search and Discovery Article #30392*, 1-72.

Boggs, S. (2006). *Principles of sedimentology and stratigraphy* (Fourth Ed.). Upper Saddle River, NJ: Prentice Hall.

Bouma, A. H. (1962). Sedimentology of some flysch deposits: a graphic approach to facies Interpretation. *Elsevier Pub. Co*.

Bromley, R.G., & Ekdale, A.A (1984). Chondrites: a trace fossil indicator of anoxia in sediments. *Science, 224*, 872–874.

Broadhead, R. F. (2015). The Upper Mancos Shale in the San Juan Basin: three plays, conventional and unconventional. *Search and Discovery, 10791*, 1–39.

Campbell, C.V. (1966). Truncated wave-ripple laminae. *Journal of Sedimentary Petrology, 36*(3), 825-828.

Campbell, C.V. (1971). Depositional Model – Upper Cretaceous Gallup Beach Shoreline, Ship Rock Area, Northwestern New Mexico. *Journal of Sedimentary Petrology, 41*(2), 395-409.

Christidis, G.E., & Huff, W.D. (2009). Geological Aspects and Genesis of Bentonites. *Elements, 5*, 93-98.

Cobban, W.A., Merewether, E.A., Fouch, T.D., & Obradovich, J.D. (1994). Some Cretaceous shorelines in the Western Interior of the United States. *The Rocky Mountain Section SEPM*, 393-414.

Correggiari, A., Cattaneo, A., & Trincardi, F. (2005). Depositional Patterns in the Late Holocene Po Delta System: River Deltas-Concepts, Models, and Examples. *SEPM Special Publication*, 365–392.

Dalrymple, R. W. (2010). Tidal Depositional Systems, in N. P. James, and R. W. Dalrymple, eds., Facies Models 4. *St. John's, Geological Association of Canada*, 201–231.

Dalrymple, R. W., Baker, E. K., Harris, P. T., & Hughes, M. G. (2003). Sedimentology and stratigraphy of a tide-dominated, foreland-basin delta (Fly River, Papua New Guinea). *Special Publication - Society for Sedimentary Geology, 76*, 147–173.

Dane, C.H., Bachman, G.O., & Reeside, J.B, JR. (1957). The Gallup Sandstone, its age and stratigraphic relationships south and east of the type locality. *Geology of Southwestern San Juan Basin, Second Field Conference*, 99-113.

DeCelles, P.G. (1994). Late Cretaceous-Paleocene synorogenic sedimentation and kinematic history of the Sevier thrust belt, northeast Utah and southwest Wyoming. *Geological Society of America Bulletin, 106,* 32-56.

DeCelles, P.G. (2004). Late Jurassic to Eocene evolution of the Cordilleran thrust belt and foreland basin system, western U.S.A. *American Journal of Science, 304*, 105–168.

DeCelles, P.G., & Giles, K.A. (1996). Foreland basin sustems. *Basin Research, 8*, 105-123.

DeReuil, A.A., & Birgenheier, L.P. (2018). Sediment dispersal and organic carbon preservation in a dynamic mudstone-dominated system, Juana Lopez Member, Mancos Shale. *Sedimentology*, https://doi.org/10.1111/sed.12532

Duke, W.L. (1985). Hummocky cross-stratification, tropical hurricanes, and intense winter storms. *Sedimentology, 32*, 167-194.

Duke, W. L. (1990). Geostrophic Circulation or Shallow Marine Turbidity Currents? The Dilemma of Paleoflow Patterns in Storm-Influenced Prograding Shoreline Systems. *Journal of Sedimentary Petrology, 60*(6), 870–883.

Duke, W.L., Arnott R.W.C., & Cheel, R.J. (1991). Shelf sandstones and hummocky cross

stratification: new insights on a stormy debate. *Geology, 19*(6), 625-628.

Eaton, J.G. (1991). Biastratigraphis framework for the Upper Cretaceous rocks of the

Kaiparowits Plateau, southern Utah. *Geological Society of America Special Paper, 260.*

Ericksen, M.C., & Slingerland, R.L. (1990). Numerical simulations of tidal and wind-driven

circulation in the cretaceous interior seaway of North America. *Geological Society of*

America Bulletin, 102, 1499–1516.

Fielding, C.R. (2010). Planform and facies variability in asymmetric deltas: facies analysis and

depositional architecture of the Turonian Ferron sandstone in the western Henry

Mountains, south-central Utah, U.S.A. *Journal of Sedimentary Research, 80*, 455-479. .

Fischer, A.G., Herbert, T., & Premoli-Silva, L. (1985). Fine-Grained Deposits and Biofacies of

the Cretaceous Western Interior Seaway: Evidence of Cyclic Sedimentary Processes.

SEPM Field Trip Guidebook 4, 1-10.

Fluteau, F., Remstein, G., Besse, J., Guiraud, R., & Masse, J.P. (2007). Impacts of

Palaeogeography and sea level changes on Mid-Cretaceous climate. *Palaeogeography,*

Palaeoclimatology, Palaeoecology, 247, 357-381.

Frey, R.W., Pemberton S.G., & Saunders, T.D.A (1990). Ichnofacies and bathymetry: a passive

relationship. *Journal of Paleontology, 64*(1), 155-158.

Friedrichs, C.T., & Wright, L.D. (2004). Gravity-driven sediment transport on the continental

shelf: implications for equilibrium profiles near river mouths. *Coastal Engineering, 51*,

795-811.

Friedrichs, C.T., & Scully, M.E. (2007). Modeling deposition by wave-supported gravity flows

on the Po River prodelta: from seasonal floods to prograding clinoforms. *Continental*

Shelf Research, 27, 322–337.

Gale, A.S., Hardenbol, J., Hathway, B., Kennedy, W.J., Young, J.R., & Phansalkar, V. (2002). Global correlation of Cenomanian (Upper Cretaceous) sequences: Evidence for Milankovitch control on sea level. *Geology, 30*(4), 291-294.

Garrison, J. R., Jr., & van de Bergh, T.C.V. (2004). High-resolution depositional sequence stratigraphy of the upper ferron sandstone last chance delta; an application of coal-zone stratigraphy. *AAPG Studies in Geology, 50*, 125-192.

Garvine, R.W. (1982). A steady state model for buoyant surface plum hydrodynamics in coastal waters. *Tellus*, *34*, 293-306.

Gingras, M.K., Pemberton S.G., & Smith, M. (2015). Bioturbation: reworking sediments for better or worse. *Oilfield Review Winter 2014/2015, 26*(4), 46-58.

Hampson, G.J. (2010). Sediment dispersal and quantitative stratigraphic architecture across an ancient shelf. *Sedimentology, 57*, 96–141.

Haq, B.U. (2014). Cretaceous eustasy revisited. *Global and Planetary Change 113*, 44–58.

Harazim, D., & McIlroy, D. (2015). Mud-rich density-driven flows along an early Ordovician storm-dominated shoreline: implications for shallow-marine facies models. *Journal of Sedimentary Research, 85*, 509–528.

Harms, J.C., Southard, J.B., Spearing, D.R., & Walker, R.G. (1975). Depositional environments as interpreted from primary sedimentary structures and stratification sequences. *Society of Economic Paleontologists and Mineralogists, Short Course 2.*

Hart, B. S. (2016). Marine mudstone source rocks in epicontinental basins: Development of a conceptual facies model and application to Cenomanian/Turonian mudstones of the Cretaceous Western Interior Seaway, in M. P. Dolan, D. K. Higley, and P. G. Lillis, eds., Hydrocarbon Source Rocks in Unconventional Plays, Rocky Mountain Region, 364

421.

Hay, W.W. (2008). Evolving ideas about the Cretaceous climate and ocean circulation. *Cretaceous Research 29*, 725–753.

He, S., Kyser, T.K., & Caldwell, W.G.E. (2005). Plaeoenvironment of the Western Interior Seaway inferred from $\delta^{18}O$ and $\delta^{13}C$ values of molluscs from the Cretaceous Bearpaw marine cyclothem. *Palaeogeography, Palaeoclimatology, Palaeoecology, 217*, 67-85.

Hovikoski, J., Lemiski, R., Gingras, M., Pemberton, G., & MacEachern, J.A. (2008). Ichnology and Sedimentology of a mud-dominated deltaic coast: Upper Cretaceous Alderson Member (Lea Park Fm), Western Canada. *Journal of Sedimentary Research, 78*, 803-824.

Hu, Y. (1997). High-resolution sequence stratigraphic analysis of the Upper Cretaceous Puskwaskau Formation of west-central Alberta and adjacent B.C.: outcrop and subsurface. Unpub. Ph. D. thesis, University of Western Ontario, London, Canada, 309p.

Hu, X., Wagreich, M., & Yilmaz, I.O. (2012). Marine rapid environmental/climatic change in the Cretaceous greenhouse world. *Cretaceous Research, 38*, 1-6.

Johnson, R.C. (2003). Depositional framework of the Upper Cretaceous Mancos Shale and the lower part of the Upper Cretaceous Mesaverde Group, western Colorado and eastern Utah. *Petroleum Systems and Geologic Assessment of Oil and Gas in the Uinta–Piceance Province, Utah and Colorado: United States Geological Survey, Digital Data Series DDS 69-B*.

Joo, Y.J., & Sageman, B.B. (2014). Cenomanian to Campanian carbon isotope chemostratigraphy from the Western Interior Basin, U.S.A. *Journal of Sedimentary Research, 84*, 529-542.

Kane, I.A., Kneller, B.C., Dykstra, M., Kassem, A., & McCaffrey, W.D. (2007). Anatomy of a

submarine channel-levee: an example from Upper Cretacaous slope sediments, Rosario Formation, Baja California, Mexico. *Marine and Petroleum Geology, 24*, 540-563.

Kauffman, E.G. (1977). Geological and biological overview: Western Interior Cretaceous Basin. *The Mountain Geologist, 14*(3-4), 75-99.

Kauffman, E.G. (1984). Dynamic paleobiogeography and evolutionary response in the Cretaceous Western Interior of North America, in WESTERMANN, G.E.G., ed.,Jurassic Cretaceous Biochronology and Paleogeography of North America. *Geological Association Canada Special, 27*, 273-306.

Kauffman, E.G. (1985). Cretaceous evolution of the Western Interior basin of the United States. Fine-Grained Deposits and Biofacies of the Cretaceous Western Interior Seaway: Evidence of Cyclic Sedimentary Processes. *SEPM, Field Trip Guidebook, 4*.

Kauffman, E.G., & Caldwell, W.G.E. (1993). The Western Interior Basin in space and time. In: Caldwell, W.G.E., Kauffman, E.G. (Eds.), Evolution of the Western Interior Basin. *Geological Association of Canada Special Paper, Toronto, ON, pp. 1–30.*

Kineke, G.C.C., Sternberg, R.W.W., Trowbridge, J.H.H. & Geyer, W.R.R. (1996). Fluid-mud processes on the Amazon continental shelf. Continental Shelf Research, 16(5–6), 667-696.

Krueger, R. (2010). Strike variability within a wave-influenced delta, the Gallup Sandstone, Shiprock, New Mexico. University of Houston, MS Thesis, 116p.

Kuehl, S. A., Levy, B. M., Moore, W. S., & Allison, M. A. (1997). Subaqueous delta of the Ganges-Brahmaputra river system. *Marine Geology, 144*(1-3), 81-96.

Lamb, G.M. (1973). The Lower Mancos Shale in the Northern San Juan Basin. *Four Corners Geological Society Memoir Book,* 72-77.

Laurin, J., & Sageman, B.S. (2007). Cenomanian–Turonian Coastal Record in SW Utah, U.S.A.: orbital-scale transgressive–regressive events during oceanic anoxic event II. *Journal of Sedimentary Research, 77*, 731–756.

Leithold, E.L. (1994). Stratigraphical architecture at the muddy margin of the Cretaceous Western Interior Seaway, southern Utah. *Sedimentology, 41*(3), 521-542.

Li, Z., Bhattacharya, J.P., & Schieber, J. (2015). Evaluating along-strike variation using thin-bedded facies analysis, Upper Cretaceous Ferron Notom Delta, Utah. *Sedimentology, 67*, 2060-2089.

Liu, J.P., Li., A.C., Xu., K.H., Velozzi, D.M., Yang, Z.S., Milliman, J.D., & DeMaster, D.J. (2006). Sedimentary features of the Yangtze River-derived along-shelf clinoform deposit in the East China Sea. *Continental Shelf Research, 26*, 2141-2156.

Liu, J. P., Xu, K. H., Li, A. E. A., Milliman, J. D., Velozzi, D. M., Xiao, S. B., & Yang, Z. S. (2007). Flux and fate of Yangtze River sediment delivered to the East China Sea. *Geomorphology, 85*(3-4), 208-224.

Liu, J.P., Hsu, R.T., Yang, R.J., Ping Wang, Y., Wu, H., Du, X., Li, A., Chien , S.C., Lee, J., Yang, S., Zhu, J., Su, C., Chang, Y., & Huh, C. (2018). A comprehensive sediment dynamics study of a major mud belt system on the inner shelf along an energetic coast. *Scientific Reports, 8*, 4229.

Livaccari, R.F. (1991). Role of crustal thickening and extensional collapse in the tectonic evolution of the Sevier-Laramide orogeny, western United States. *Geology, 19*, 1104-1107.

Lock, B.E., Butler, R.W., & Franklund, R.T. (2009). Tempestite sedimentation: An example from the Del Rio Formation of West Texas. *Gulf Coast Association of Geological*

Societies Transactions, 59, 463-476.

Lowe, D.R. (1979). Sediment gravity flows: their classification and some problems of application to natural flows and deposits. *SEPM Special Publication,* (2), 27-82.

MacEachern, J.A., Bann, K.L., Bhattacharya, J.P., & Howell, C.D. (2005). Ichnology of deltas: organism responses to the dynamic interplay of rivers, waves, storms, and tides. *SEPM Special Publication 83*, 49-85.

Mack, G.H., Hook, S., Giles, K.A., & Cobban, W.A. (2015). Sequence stratigraphy of the Mancos Shale, lower Tres Hermanos Formation, and coeval middle Cenomanian to middle Turonian strata, southern New Mexico, USA. *Sedimentology*.

MacKay, D.A., & Dalrymple, R.W. (2011). Dynamic mud deposition in a tidal environment: the record of fluid-mud deposition in the Cretaceous Bluesky Formation, Alberta, Canada. *Journal of Sedimentary Research, 81*, 901-920.

Macquaker, J.H.S., & Bohacs, K.M. (2007). On the accumulation of mud. *Science, 318*, 1734-1735.

Macquaker, J.H.S., Bentley, S.J., & Bohacs, K.M. (2010). Wave-enhanced sediment-gravity flows and mud dispersal across continental shelves: Reappraising sediment transport processes operating in ancient mudstone successions. *Geology, 38*(10), 947-950.

Markwick, P.J., & Rowley, D.B. (1998). The geological evidence for Triassic to Pleistocene Glaciations; implications for eustasy. *Society for Sedimentary Geology, 58,* 17-43.

Martin, K.D. (2004). A re-evaluation of the relationship between trace fossils and dysoxia, in McIlroy, D., ed., The Application of Ichnology to Palaeoenvironmental and Stratigraphic Analysis. *Geological Society of London, Special Publication, 228*, 141–156.

McCool, W.W., & Parsons, J.D. (2004). Sedimentation from buoyant fine-grained suspensions.

Continental Shelf Research, 24, 1129-1142.

McCubbin, D.G. (1982). Barrier-island and strand-plain facies. *Memoir - American Association of Petroleum Geologists*, *31*, 247-279.

Middleton, G. (1973). Johannes Walther's Law of Correlation of Facies. *Geological Society of America Bulletin*, *38*, 979-988.

Miller, K.G., Sugarman, P.J., Browning, J.V., Kominz, M.A., Hernandez, J.C., Olsson, R.K., Wright, J.D., Feigenson, M.D., & Van Sickel, W. (2003). A chronology of Late Cretaceous sequences and sea-level history: glacioeustasy during the Greenhoouse World. *Geology, 31*, 585–588.

Miller, K.G., Sugarman, P.J., Browning, J.V., Kominz, M.A., Olsson, R.K., Feigenson, M.D., & Hernandez, J.C. (2004). Upper Cretaceous sequences and sea-level history, New Jersey Coastal Plain. *Geological Society of America Bulletin, 116*, 368–393.

Miller, K.G., Wright, J.D., Browning, J.V., Kominz, M.A., & Sugarman, P.J. (2005). Visions of ice sheets in a greenhouse world. *Marine Geology, 217,* 215-231.

Molenaar, C.M. (1973). Sedimentary facies and correlations of Gallup Sandstone and associated formations, northwestern New Mexico. *The American Association of Petroleum Geologists Bulletin, 57*(5), 959.

Molenaar, C.M. (1977). Stratigraphy and depositional history of Upper Cretaceous rocks of the San Juan Basin area, New Mexico and Colorado, with a note on economic resources. New Mexico Geological Society Guidebook, 28th Field Conference, 159–166.

Molenaar, C.M. (1983). Principal reference section and correlation of Gallup Sandstone, northwestern New Mexico, in S.C. Hook, compiler, Contributions to mid-Cretaceous paleontology and stratigraphy of New Mexico. *New Mexico Bureau of Mines and*

Mineral Resources Circular, 185, 29–40.

Molenaar, C.M.,& Cobban,W.A. (1991). Middle Cretaceous stratigraphy on the south and east

    sides of the Uinta Basin, northeastern Utah and northwestern Colorado. 1787P.

Morehead, M.D., & Syvitski, J.P. (1999). River-plume sedimentation modeling for sequence

    stratigraphy: application to the Eel margin, northern California. *Marine Geology, 154*,

    29-41.

Mulder, T., & Syvitski, J.P.M. (1995). Turbidity currents generated at river mouths during

    exceptional discharges to the world oceans. *The Journal of Geology*, 285-299.

Mulder, T., Syvitski, J.P.M., Migeon, S., Faugères, J.C., & Savoye, B. (2003). Marine

    hyperpycnal flows: initiation, behavior and related deposits. *Marine and*

    Petroleum Geology, 20(6-8), 861-882.

Myrow, P.M., Fischer, W., & Goodge, J.W. (2002). Wave-modified turbidites: combined-flow

    shoreline and shelf deposits, Cambrian, Antarctica: *Journal of Sedimentary Research, 72*

    (5), 641-656.

Myrow, P.M., Lukens, C., Lamb, M.P., Houck, K., & Strauss, J. (2008). Dynamics of a

    transgressive prodeltaic system: implications for geography and climate within a

    Pennsylvanian intracratonic basin, Colorado, USA. *Journal of Sedimentary Research, v.*

    78(8), 512-528.

Nichols, G. (2009). *Sedimentology and Stratigraphy* (Second Ed.). Oxford, UK; Wiley-

    Blackwell.

Nio, S.-D., & Yang, C.-D. (1991). Diagnostic attributes of clastic tidal deposits: a review, in D.

    G. Smith, G. E. Reinson, B. A. Zaitlin, and R. A. Rahmani, eds., Clastic Tidal

    Sedimentology. *Canadian Society of Petroleum Geologists, Memoir 16*, 3–28.

Nittrouer, C. A., Kuehl, S.A., Figueiredo, A.G., Allison, M.A., Sommerfield, C.K., Rine, J.M.,
  Faria, L.E.C., & Silveira, O.M. (1996). The geological record preserved by Amazon shelf
  Sedimentation. *Continental Shelf Research, 16*(5–6), 817–841.

Normark, W.R., & Piper, D.J. (1991). Initiation processes and flow evolution of turbidity
  currents: implications for the depositional record. *SEPM Special Publication, 46*,
  207-230.

Nummedal, D. (1990). Sequence stratigraphic analysis of upper Turonian and Coniacian strata in
  the San Juan basin, New Mexico, U.S.A., in R.N. Ginsburg and B. Beaudoin, eds.,
  Cretaceous resources, events and rhythms. *Dordrecht, Kluwer Publishing*, 33–46.

Nummedal, D., & Molenaar, C.M. (1995). Sequence Stratigraphy of Ramp-Setting Strand Plain
  Successions: The Gallup Sandstone, New Mexico. 277-310.

Orton, G. J., & Reading, H. G. (1993). Variability of deltaic processes in terms of sediment
  supply, with particular emphasis on grain size. *Sedimentology, 40*(3), 475-512.

Passey, Q. R., Dahlberg, K.E., Sullivan, K., Yin, H., Brackett, B., Xiao, Y., & Guzman-
  Garcia, A.G. (2006). Definitions and Geological Occurence of Thin Beds in Clastics.
  AAPG Archie Series, 1, 26–39.

Pattison, S.A.J. (2005). Storm-Influenced Prodelta Turbidite Complex in the Lower Kenilworth
  Member at Hatch Mesa, Book Cliffs, Utah, U.S.A.: Implications for Shallow Marine
  Facies Models. *Journal of Sedimentary Research, 75*(3), 420–439.

Pattison, S.A.J., Ainsworth R.B., & Hoffman, T.A. (2007). Evidence of across‐shelf transport
  of fine‐grained sediments: turbidite‐filled shelf channels in the Campanian Aberdeen
  Member, Book Cliffs, Utah, USA. *Sedimentology, 54*(5), 1033-1064.

Pemberton, S.G., Van Wagoner, J.C., & Wach, G.D. (1992). Ichnofacies of a wave-dominated

shoreline. *SEPM Special Publication,* 339-382.

Pentilla, W.C., (1964). Evidence for the pre-Niobrara unconformity in the northwestern part of

the San Juan Basin. *The Mountain Geologist, 1*(1), 3-14.

Peterson, F., & Ryder, R. T. (1975). Cretaceous rocks in the Henry Mountains region, Utah and

their relation to neighboring regions; in Fassett, J. E., and Wengerd, S. A. (eds.),

Canyonlands Country. *Four Corners Geological Society Guidebook, 8th Field*

Conference, 167-189.

Peterson, F., Ryder, R. T., & Law, B. E. (1980). Stratigraphy sedimentology and regional

relationships of the Cretaceous System in the Henry Mountains region, Utah. *Utah*

Geological Society Guidebook, 1980, Henry Mountains Symposium, 151-170.

Plint, A.G. (1991). High-frequency relative sea-level oscillations in Upper Cretaceous shelf

clastics of the Alberta foreland basin: possible evidence for glacio-eustatic control? *Spec.*

Publs. int. Ass. Sediment., 12, 409-428.

Plint, A.G. (2014). Mud dispersal across a Cretaceous prodelta: Storm-generated wave-enhanced

Sediment gravity flows inferred from mudstone microtexture and microfacies.

Sedimentology, 61, 609–647.

Plint, A.G., Macquaker, J.H.S., & Verban, B.I. (2012). Bedload transport of mud across a wide,

storm-influenced ramp: Cenomanian–Turonian Kaskapau Formation, Western Canada

Foreland Basin. *Journal of Sedimentary Research, 82*, 801-822.

Rankin, C.H. (1944). Stratigraphy of the Colorado Group, Upper Cretaceous in northern New

Mexico. *New Mexico Bur. Mines and Mineral Resources Bull., 20*, 1-26.

Rebesco, M., Hernandez-Molina, F.J., Rooij, D.V., & Wahlin, A. (2014). Contourites and

associated sediments controlled by deep-water circulation processes: State-of-the-art and

future considerations. *Marine Geology, 352*, 111-154

Rhoads, D.C., & Morse, J.W. (1971). Evolutionary and ecologic significance of oxygen-deficient marine basins. *Lethaia, 4*, 413–428.

Ridgley, J.L., Condon, S.M., & Hatch, J.R. (2013). Geology and Oil and Gas Assessment of the Mancos-Menefee Composite Total Petroleum System. *U.S. Geological Survey Digital Data Series, 69*, 1-97.

Sageman, B.B., & Arthur, M.A. (1994). Early Turonian paleogeographic/paleobathymetric map, Western Interior, U.S. In: C. M., P. J. (Ed.), Mesozoic Systems of the Rocky Mountain Region. Rocky Mountain Section. *SEPM Special Publication, United States*, 457–470.

Sanders, J.E. (1960). Primary sedimentary strictures formed by turbidity currents and related resedimentation mechanisms. *SEPM*, 192-219.

Savin, S.M. (1977). The history of the earth's surface temperature during the past 100 million years. *Ann. Rev. Earth Planet. Sci., 5*, 319-355.

Savrda, C.E., & Bottjer, D.J. (1987). The exaerobic zone, a new oxygen-deficient marine biofacies. *Nature, 327*, 54–56.

Sealey, P.L, Lucas, S.G., Spielmann, J.A., & Williams, S.C. (2006). Upper Cretaceous (Turonian) ammonites and selachians from the type area of the Juana Lopez Member of the Mancos Shale, Santa Fe County, New Mexico. *New Mexico Museum of Natural History and Science Bulletin, 35*, 131-138.

Schieber, J. (2016). Mud re-distribution in epicontinental basins - Exploring likely processes. *Marine and Petroleum Geology, 71*, p. 119–133.

Schieber, J. (2011). Reverse engineering mother nature - shale sedimentology from an experimental perspective. *Sedimentary Geology, 238*, 1–22.

Schieber, J., Southard, J., & Thaisen, K. (2007). Accretion of mudstone beds from migrating floccule ripples. *Science, 318*, 1760–1763.

Schieber, J., & Southard, J.B. (2009). Bedload transporschot ofmud by floccule ripples—direct observation of ripple migration processes and their implications. *Geology, 37*, 483–486.

Schwarzacher, W., & Fischer, A. G. (1982). Limestone-shale bedding and perturbations of the Earth's orbit. *Cyclic and event stratification,* 72-95.

Seilacher, A. (1967). Bathymetry of trace fossils. *Marine Geology, 5*(5-6), 413-428.

Seilacher, A. (1984). Storm beds: Their significance in event stratigraphy. 49-54.

Shanley, K.W., & McCabe, P.J. (1991). Predicting facies architecture through sequence stratigraphy- An example from the Kaiparowits Plateau, Utah. *Geology, 19*, 742-745.

Slingerland, R., & Keen, T.R. (1999). Sediment transport in the Western Interior Seaway of North America; predictions from a climate-ocean-sediment model. In: Bergman, K.M., Snedden, J.W. (Eds.), Isolated Shallow Marine Sand Bodies. *SEPM Special Publication*, 179–190.

Stow, D.A.V., Kahler, G., & Reeder, M., (2002). Fossil contourites: type example from an Oligocene palaeoslope system, Cyprus. In: Stow, D.A.V., Pudsey, C.J., Howe, J.A., Faugères, J.-C., Viana, A.R. (Eds.), Deep-water Contourite Systems: Modern Drifts and Ancient Series, Seismic and Sedimentary Characteristics. *Geological Society, London, Memoir, 22*, 443–455.

Swift, D.J.P., Figueiredo Jr., A.G., Freeland, G.L., & Oertel, G.F. (1983) Hummocky cross stratification and megaripples: a geological double standard? Journal of Sedimentary *Petrology, 53*(4), 1295-1317.

Taylor, A.M., & Goldring, R. (1993). Description and analysis of bioturbation and ichnofabric.

Journal of the Geological Society of London, 150, 141–148.

Traykovski, P., Geyer, W.R, Irish, J.D., & Lynch, J.F. (2000). The role of wave-induced density driven fluid mud flows for cross-shelf transport on the Eel River continental shelf. *Continental Shelf Research, 20*(16), 2113-2140.

Walther, J. (1894). Einleitung in die Geologie als historische Wissenschaft. *Lithogenesis der Gegenwart. Jena: G. Fischer*, *3*, 535-1055.

Weimer, R.J. (1984). Relation of unconformities, tectonics, and sea-level changes, Cretaceous of Western Interior, U.S.A. In: Schlee, J.S. (Ed.), Interregional Unconformities and Hydrocarbon Accumulation. *American Association of Petroleum Geologists, Tulsa, OK, United States*, 7–35.

Wignall, P.B. (1991) Dysaerobic trace fossils and ichnofabric in the Upper Jurassic Kimmeridge Clay of southern England. *Palaios, 6,* 264–270.

Wignall, P.B., & Pickering, K.T., (1993). Paleoecology and sedimentology across a Jurassic fault scarp, northeast Scotland. *Geological Society of London, Journal, 150*, 323–340.

Wilson, R.D., & Schieber, J. (2014). Muddy hyperpycnites in the Lower Genesee Group of Central New York, USA: implications for mud transport in epicontinental seas. *Journal of Sedimentary Research., 84*, 866–874.

Wilson, R.D., & Schieber, J. (2015). Sedimentary facies and depositional environment of the middle Devonian Geneseo formation of New York, U.S.A. *Journal of Sedimentary Research, 85*, 1393–1415.

Yawar, Z., & Schieber, J. (2017). On the origin of silt laminae in laminated shales. *Sedimentary Geology, 360*, 22–34.

Yonkee, W.A., & Weil, A.B. (2015). Tectonic evolution of the Sevier and Laramide belts within

the North American Cordillera orogenic system. *Earth-Science Reviews, 150*, 531-593.

Zhu, Y., Bhattacharya, J.P., Li, W., Lapen, T.J., Jicha, B., & Singer, B. (2012). Milankovitch-
Scale Sequence Stratigraphy and Stepped Forced Regressions of the Turonian Ferron
Notom Deltaic Complex, South-Central Utah, U.S.A., *Journal of Sedimentary Research,
82*, 723-746.
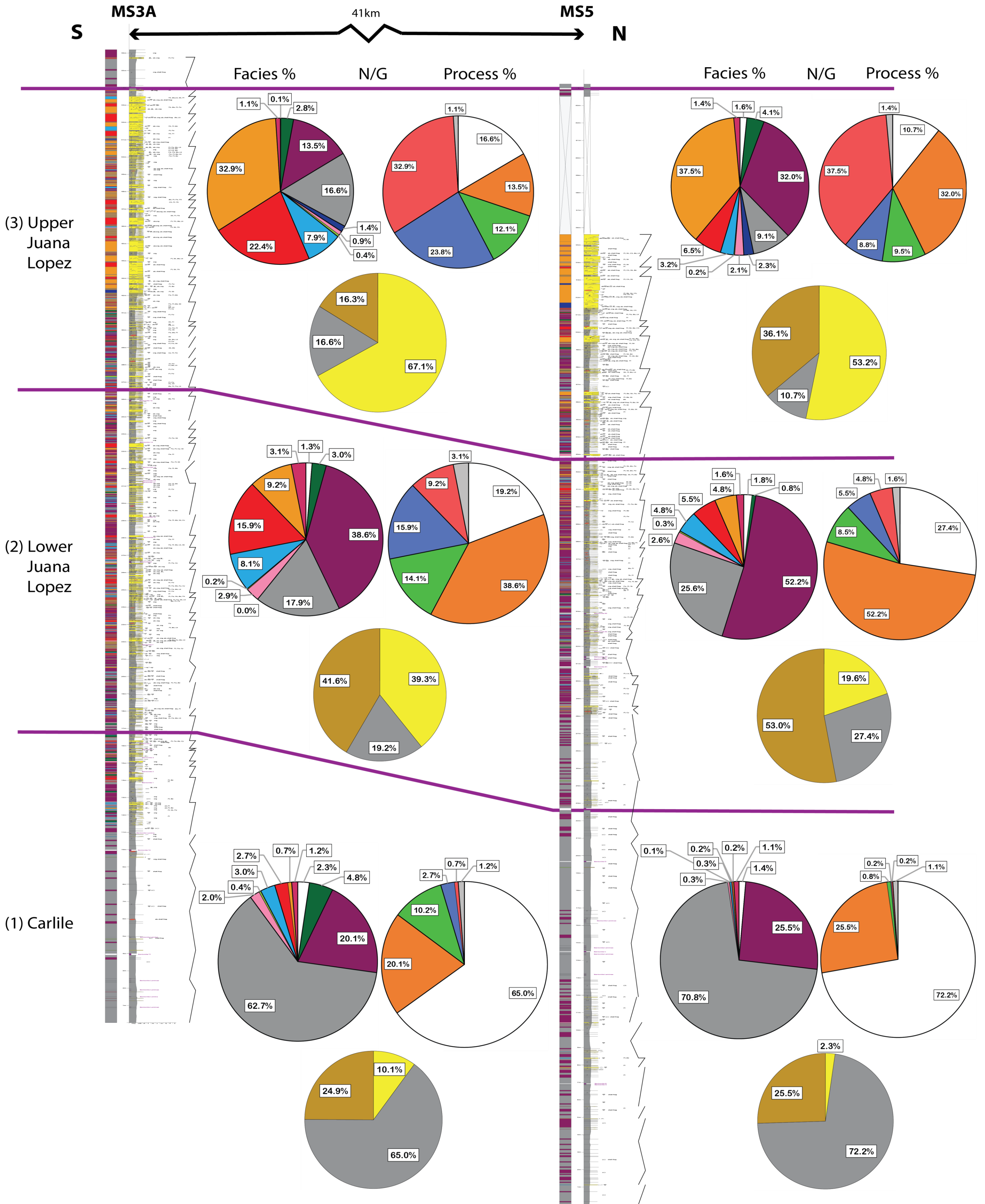
Poster 1 – Poster size of Figure 23.

Poster 2 – Poster size of Figure 24.

Poster 3 – Poster size of Figure 27.